microLife, 2025, **6**, uqae024
DOI: 10.1093/femsml/uqae024
Advance access publication date: 5 December 2024
Research Article

The proteomic response of *Aspergillus fumigatus* to amphotericin B (AmB) reveals the involvement of the RTA-like protein RtaA in AmB resistance

Ammar Abou-Kandil[1,‡], Sophie Tröger-Görler[2,‡], Annica Pschibul[2,‡], Thomas Krüger[2], Maira Rosin[2,3], Franziska Schmidt[2,3], Parastoo Akbarimoghaddam[4], Arjun Sarkar[4], Zoltán Cseresnyés[4], Yana Shadkchan[1], Thorsten Heinekamp[2], Markus H. Gräler[5,6,7], Amelia E. Barber[3,8], Grit Walther[9], Marc Thilo Figge[3,4], Axel A. Brakhage[2,3], Nir Osherov[1,*], Olaf Kniemeyer[2,*]

[1]Tel-Aviv University, Department of Clinical Microbiology and Immunology, Faculty of Medical and Health Sciences, Ramat-Aviv, 69987 Tel-Aviv, Israel
[2]Department of Molecular and Applied Microbiology, Leibniz Institute for Natural Product Research and Infection Biology, Hans Knöll Institute (HKI), Adolf-Reichwein-Str. 23, 07745 Jena, Germany
[3]Institute of Microbiology, Friedrich Schiller University (FSU), 07743 Jena, Germany
[4]Research Group Applied Systems Biology, Leibniz Institute for Natural Product Research and Infection Biology (HKI), 07745 Jena, Germany
[5]Department of Anesthesiology and Intensive Care Medicine, Jena University Hospital, 07747 Jena, Germany
[6]Center for Molecular Biomedicine (CMB), Jena University Hospital, 07745 Jena, Germany
[7]Center for Sepsis Control and Care (CSCC), Jena University Hospital, 07747 Jena, Germany
[8]Junior Research Group Fungal Informatics, Friedrich Schiller University, 07745 Jena, Germany
[9]National Reference Centre for Invasive Fungal Infections (NRZMyk), 07745 Jena, Germany
*Corresponding authors. Olaf Kniemeyer, Department of Molecular and Applied Microbiology, Leibniz Institute for Natural Product Research and Infection Biology, Hans Knöll Institute (Leibniz-HKI), Adolf-Reichwein-Str. 23, 07745 Jena. Germany, E-mail: olaf.kniemeyer@leibniz-hki.de; Nir Osherov, Department of Clinical Microbiology and Immunology, Faculty of Medical and Health Sciences, Tel Aviv University, Ramat Aviv, 69987 Tel Aviv, Israel. E-mail: nosherov@post.tau.ac.il
‡These authors contributed equally to this study
Editor: [Carmen Buchrieser]

Abstract

The polyene antimycotic amphotericin B (AmB) and its liposomal formulation AmBisome belong to the treatment options of invasive aspergillosis caused by *Aspergillus fumigatus*. Increasing resistance to AmB in clinical isolates of *Aspergillus* species is a growing concern, but mechanisms of AmB resistance remain unclear. In this study, we conducted a proteomic analysis of *A. fumigatus* exposed to sublethal concentrations of AmB and AmBisome. Both antifungals induced significantly increased levels of proteins involved in aromatic acid metabolism, transmembrane transport, and secondary metabolite biosynthesis. One of the most upregulated proteins was RtaA, a member of the RTA-like protein family, which includes conserved fungal membrane proteins with putative functions as transporters or translocases. Accordingly, we found that RtaA is mainly located in the cytoplasmic membrane and to a minor extent in vacuolar-like structures. Deletion of *rtaA* led to increased polyene sensitivity and its overexpression resulted in modest resistance. Interestingly, *rtaA* expression was only induced by exposure to the polyenes AmB and nystatin, but not by itraconazole and caspofungin. Orthologues of *rtaA* were also induced by AmB exposure in *A. lentulus* and *A. terreus*. Deletion of *rtaA* did not significantly change the ergosterol content of *A. fumigatus*, but decreased fluorescence intensity of the sterol-binding stain filipin. This suggests that RtaA is involved in sterol and lipid trafficking, possibly by transporting the target ergosterol to or from lipid droplets. These findings reveal the contribution of RtaA to polyene resistance in *A. fumigatus*, and thus provide a new putative target for antifungal drug development.

Keywords: *Aspergillus fumigatus*; drug resistance; proteomics; antifungals; membrane protein; amphotericin B

Introduction

Human health is seriously threatened by fungal infections. These eukaryotic pathogens kill about 2.5 million people per year and infect billions of people globally, ranking on par with well-known bacterial or protozoan pathogens like those that cause tuberculosis or malaria (Brown et al. 2012, Denning 2024). Fungal infections are notoriously challenging to treat. Amphotericin B (AmB), a polyene macrolide antibiotic initially isolated from the soil bacterium *Streptomyces nodosus*, has been the preferred antifungal medication for treating various systemic mycotic infections over the past six decades (Carolus et al. 2020). The drug is administered intravenously, either as a conventional form complexed to sodium deoxycholate or as a liposomal formulation called AmBisome, which enhances its solubility and availability. AmB exerts its antifungal activity by binding to ergosterol, a key component of fungal cell membranes, which leads to pore formation, ergosterol sequestration, and ultimately cell death due to oxidative stress and loss of membrane integrity (Cavassin et al. 2021). Compared to other antifungal agents, AmB has demonstrated lower rates of resistance due to its fungicidal properties and its ability to target ergosterol, a metabolic product, rather than specific enzymes involved in its biosynthesis (Goncalves et al. 2016, Carolus et al. 2020). The development of resistance to AmB often incurs a significant cost to fungal fitness, as seen in previous studies (Vincent et al. 2013). The most frequent cause of acquired AmB resistance is alterations in the sterol composition of the fungal cell

Received 20 June 2024; **revised** 19 November 2024; **accepted** 4 December 2024

membrane, which results in the loss of the drug target ergosterol. In *Candida* species, resistance has been linked to genetic mutations in enzymes involved in ergosterol biosynthesis (Martel et al. 2010, Vincent et al. 2013, Ahmad et al. 2019).

AmB and AmBisome are widely used for empirical and salvage treatment of invasive pulmonary aspergillosis (IPA), one of the most severe fungal infections, with mortality rates that can reach up to 90% (Arastehfar et al. 2021). IPA is predominantly caused by inhalation of *Aspergillus fumigatus* spores (conidia), a saprophytic mold commonly found in the environment. In immunocompromised individuals, inhaled conidia can germinate and cause fatal invasive disease. Despite recent reports indicating high resistance rates in clinical isolates of *Aspergillus* species (*A. terreus*, *A. flavus*, *A. niger*, *A. lentulus*, and *A. fumigatus*), the mechanisms of AmB resistance in *Aspergilli* are not well understood, raising concerns about the efficacy of AmB as a therapeutic option for IPA (Ashu et al. 2018, Reichert-Lima et al. 2018, Imbert et al. 2020, Fakhim et al. 2022). Therefore, understanding the mechanisms of AmB resistance in *A. fumigatus* is a pressing need to enable the creation of novel resistance-evading treatment approaches. However, research on this issue has been limited. Manavathu et al. (1998) generated *A. fumigatus* AmB-resistant isolates by UV irradiation but did not identify the responsible genetic drivers. Furukawa et al. (2020) recently demonstrated that deletion of the negative cofactor 2 transcriptional regulators encoded by *nctA* and *nctB* leads to AmB resistance, but the underlying mechanisms are not fully understood. Gautam et al. (2008) used a transcriptomic and 2D gel-based proteomic approach to identify differentially expressed genes and proteins, respectively, in *A. fumigatus* following 24 h exposure to AmB. However, the obtained findings, such as an increase of ergosterol biosynthetic enzymes, were not further examined for their potential to confer resistance.

To address this knowledge gap, we employed advanced analytical tools to investigate the proteomic response of *A. fumigatus* to both AmB and AmBisome, since we were also interested in whether the drug formulation affects the proteomic response. We then employed genetic and molecular methods to examine the most strongly elevated proteins. Our approach led to the identification of a novel resistance gene, *Afu3g12830* (*rtaA*), encoding a member of the RTA-like protein family putatively belonging to fungal lipid-translocating exporter proteins (Manente and Ghislain 2009). Our findings reveal that this gene plays a hitherto unknown role in generating AmB resistance, providing a new target for future antifungal drug development and shedding new light on a protein family that has hardly been studied in filamentous fungi.

Materials and methods

Strains and growth conditions

Aspergillus fumigatus strains were grown on Yeast Extract (YAG) solid medium [0.5% (w/v) yeast extract, 1% (w/v) dextrose, 0.01 M $MgSO_4$, trace elements solution, vitamin mix, 1.5% (w/v) agar] or solid *Aspergillus* minimal medium (AMM), for 48–72 h at 37°C. Conidia were harvested after 72 h in 0.02% (v/v) Tween 20 in water, then resuspended in double distilled water (DDW), and counted with a hemocytometer. Minimal inhibitory concentrations (MICs) were determined by CLSI M38-A2 broth microdilution methodology in Roswell Park Memorial Institute-3-(N-Morpholino)propansulfonsäure (RPMI–MOPS) broth [10% (v/v) RPMI × 10, 3.45% (w/v) MOPS], or in AMM (Brakhage and Van den Brulle 1995). Spot assays were performed on AMM or RPMI–MOPS agar plates. Transformation of *A. fumigatus* protoplasts was performed on Yeast extract Peptone Glucose Saccharose (YPGS) agar plates using hygromycin B selection [2% (w/v) yeast extract, 0.5% (w/v) peptone, 2% (w/v) D-glucose, 1 M sucrose, 1.5% (w/v) agar for plates or 0.7% (w/v) for top agar, 200 µg/ml hygromycin B, and pH = 6]. 0.5% (w/v) xylose (Sigma-Aldrich, Rehovot, Israel) was added to MIC and spot experiments to induce the overexpression of *rtaA* in the $RtaA^{PXylP}$ and 1% (w/v) xylose (AppliChem, Darmstadt, Germany) to induce the overexpression of *rtaA-gfp* in the $RtaA\text{-}GFP^{PXylP}$ strain. The *A. fumigatus* strains used in this study were all constructed in strain Δ*KU80* (da Silva Ferreira et al. 2006), here referred to as wild type (WT). Strains are listed in Tables S1 and S2, and their construction and verification are displayed in Tables S3 and S4, and Figs S1–S3.

The *A. terreus* strains 2023–0030, with low AmB MIC and 2023–1134 with high AmB MIC were grown on solid AMM for 72 h at 37°C. *Aspergillus lentulus* strains 2018–031 and 2019–599 with low or high AmB MIC were grown on solid AMM for 7 days at 37°C. All strains were provided by the NRZMyk (National Reference Centre for Invasive Fungal Infections, Jena, Germany) and MIC values were tested and are listed in Table S2. Conidia from all *A. terreus* and *A. lentulus* strains were harvested as described above. For expression analysis, *A. terreus* strains were grown in liquid AMM for 40 h and *A. lentulus* strains were grown for 24 h in liquid AMM.

Scattering-based growth curves were measured using the Cell Growth Quantifier (CGQ; Aquila Biolabs, Baesweiler, Germany) in order to identify concentrations of AmB and AmBisome, which did not lead to a total growth arrest, but significantly inhibited growth. Scattering was measured continuously by the CGQ and the cells were treated with compounds, or solvent for controls, at 20 h of growth. Growth measurements were continued until the culture reached the stationary growth phase.

Proteomic analysis

Fungal mycelium was harvested by filtration with miracloth (Merck Millipore, Darmstadt, Germany), washed with ultrapure water, frozen in liquid N_2 and disrupted by grinding with mortar and pestle. Protein was extracted from the ground mycelium by mixing and sonication in lysis buffer [1% (w/v) SDS, 150 mM NaCl, 100 mM TEAB with cOmplete Ultra Protease Inhibitor Cocktail and PhosSTOP (one tablet per 10 ml, Roche Diagnostics, Mannheim, Germany) and 0.33 U/µl Benzonase (Novagen, Merck, Darmstadt, Germany)] for 30 min at 37°C. Cell debris was removed by centrifugation at 14 000 × *g* for 15 min at 4°C. The protein concentration of the supernatant was determined using the Direct Detect System (Merck Millipore). 100 µg of protein in 100 µl of lysis buffer were reduced with 2 µl of 500 mM TCEP in 100 mM TEAB for 1 h at 55°C and alkylated with 2 µl alkylation buffer (625 mM iodoacetamide in 100 mM TEAB) for 30 min at room temperature (RT) in the dark. Protein samples were further purified by MeOH–chloroform–water precipitation using the protocol of Wessel and Flügge (1984). Dried protein pellets were solubilized in 100 mM TEAB and subsequently digested with 4 µg Trypsin/LysC protease mix (Promega, Walldorf, Germany) for 18 h at 37°C. Peptides were resolubilized in 0.05% trifluoroacetic acid (TFA)/2% acetonitrile (ACN) in water, filtered through a 10-kDa molecular weight cut-off spin filter (PTFE; Merck Millipore) and stored at −20°C until analysis.

Tryptic peptides were analysed on an UltiMate 3000 RSLCnano system with a QExactive HF mass spectrometer (Thermo Fisher Scientific, Waltham, MA, USA). The peptides were trapped on an Acclaim Pep Map 100 column (2 cm × 75 µm, 3 µm; Thermo Fisher Scientific) for 4 min with a flow rate of 5 µl/min and separated on

an Acclaim Pep Map RSLC nano column (50 cm × 75 µm, 2 µm; Thermo Fisher Scientific). Mobile phase gradient elution was performed as follows, with solvent A consisting of 0.1% (v/v) formic acid in water and solvent B of 0.1% (v/v) formic acid in 90:10 acetonitrile/water: 0–5 min at 4% B, 20 min at 7% B, 60 min at 10% B, 100 min at 15% B, 140 min at 25% B, 180 min at 45% B, 200 min at 65% B, 210–215 min at 96% B, and 215.1–240 min at 4% B. A Nanospray Flex Ion Source (Thermo Fisher Scientific) with a stainless steel emitter with 2.2 kV spray voltage was used to generate positively charged ions. The ions were measured in Full MS/data-dependent MS2 (Top 15) mode. Precursor ions were scanned at m/z 300–1500 at a resolution of up to 120 000 full width at half maximum (FWHM), with a maximal injection time of 120 ms and an AGC target of 3×10^6. Precursor ions with a charge state of z = 2–5 were filtered at an isolation width of m/z 1.6 amu and fragment ions were generated using N_2 in the higher-energy C-trap dissociation cell at 30% normalized collision energy. Fragment ions were scanned in a data-dependent manner with a dynamic exclusion of 30 s at 15 000 FWHM and an automated gain control target of 2×10^5; with a maximal injection time of 120 ms. A fixed first mass of m/z 120 amu was used.

MS/MS data were searched against the *A. fumigatus* Af293 genome of the *Aspergillus* Genome Database using Proteome Discoverer (PD) 2.2 and the algorithms of Mascot 2.4.1, Sequest HT (PD2.2 version), and MS Amanda 2.0. Two missed cleavages were allowed for tryptic peptides, the precursor mass tolerance was set to 10 ppm, and the fragment mass tolerance was set to 0.02 Da. The dynamic modification was oxidation of Met and acetylation of the N-terminus; static modification was cysteine carbamidomethylation. At least two peptides per protein and a strict target false discovery rate (FDR) of <1% were required for positive protein hits. Label-free protein quantification was based on the Minora algorithm of PD2.2 using a signal-to-noise ratio >5. Normalization was performed by using the total peptide amount method.

Positive protein hits identified in at least two out of three biological replicates of an experiment were further analysed. Proteins with altered abundances in AmB- or AmBisome-treated versus untreated cultures were compared using InteractiVenn (Heberle et al. 2015). Functional annotation assignment, gene ontology (GO) categorization and enrichment analysis of identified proteins were conducted in FungiFun 2.2.8 BETA (Priebe et al. 2015). Volcano plots were created with the aid of the web app VolcaNoseR (Goedhart and Luijsterburg 2020).

For the comparison of the proteome of the WT (CEA17 $\Delta akuB^{KU80}$) with the Δ*rtaA* strain, the protocol was modified in the following way:

Sample preparation was performed as mentioned above, except cysteine thiols were reduced and carbamidomethylated in one step for 30 min at 70°C by addition of each 2 µl of 500 mM TCEP [tris(2-carboxyethyl)phosphine] and 625 mM 2-chloroacetamide per 100 µg of total protein in 100 µl. Liquid chromatography tandem mass spectometry (LC–MS/MS) analysis was performed on an UltiMate 3000 RSLCnano system connected to a Orbitrap Exploris 480 mass spectrometer (both Thermo Fisher Scientific) with FAIMS. Peptide trapping for 5 min on an Acclaim Pep Map 100 column (2 cm × 75 µm, 3 µm) at 5 µl/min was followed by separation on an µPACneo 110 column. Mobile phase gradient elution of eluent A [0.1% (v/v) formic acid in water] mixed with eluent B [0.1% (v/v) formic acid in 90/10 acetonitrile/water] was performed using the following gradient: 0 min at 4% B and 750 nl/min, 10 min at 6.5% B and 750 nl/min, 12 min at 7% B and 300 nl/min, 85 min at 25% B and 300 nl/min, 130 min at 50% B and 300 nl/min, 135 min at 96% B and 300 nl/min, 138–140 min at 96% B and 750 nl/min, and 140.1–150 min at 4% B and 750 nl/min. Positively charged ions were generated at spray voltage of 2.2 kV using a stainless steel emitter attached to the Nanospray Flex Ion Source (Thermo Fisher Scientific). The quadrupole/orbitrap instrument was operated in Full MS/data-dependent MS2 mode. Precursor ions were monitored at m/z 300–1100 at a resolution of 120 000 FWHM using a maximum injection time (ITmax) of 50 ms and 300% normalized automatic gain control (AGC) target. Precursor ions with a charge state of z = 2–5 were filtered at an isolation width of m/z 4.0 amu for further fragmentation at 28% HCD collision energy. MS2 ions were scanned at 15 000 FWHM (ITmax = 40 ms, AGC = 200%). Each sample was measured in triplicate with a different compensation voltage (−42, −57, and −72 V).

Tandem mass spectra were searched against the UniProt pan proteome database of *A. fumigatus* (https://ftp.uniprot.org/pub/databases/uniprot/current_release/knowledgebase/pan_proteomes/UP000002530.fasta.gz; 2024/07/04, YYYY/MM/DD) using PD 3.1 (Thermo) and the database search algorithms (threshold search engine scores in parenthesis) Mascot 2.8 (>30), Comet (>3), MS Amanda 3.0 (>300), Sequest HT (>3) with Precursor Detector node with and without INFERYS Rescoring, and Chimerys (>2). Two missed cleavages were allowed for the tryptic digestion. The precursor mass tolerance was set to 10 ppm and the fragment mass tolerance was set to 0.02 Da. Modifications were defined as dynamic Met oxidation, phosphorylation of Ser, Thr, and Tyr, protein N-term acetylation with and without Met-loss as well as static Cys carbamidomethylation. A strict FDR <1% (peptide and protein level) was required for positive protein hits. The Percolator node of PD 3.1 and a reverse decoy database was used for *q*-value validation of spectral matches. Only rank 1 proteins and peptides of the top scored proteins were counted. Label-free protein quantification was based on the Minora algorithm of PD 3.1 using the precursor abundance based on intensity and a signal-to-noise ratio >5. Normalization was performed by using the total protein amount method. Imputation of missing quan values was applied by using abundance values of 75% of the lowest abundance identified per sample. Differential protein abundance was defined as a fold change of >2, *P*-value/ABS(log4ratio) < .05 (*P*-value/log4ratio) and at least identified in two of three replicates of the sample group with the highest abundance. Statistics and data visualization were performed with R 4.4.0 and RStudio 2024.04.0.

Antifungal susceptibility testing: determination of MICs

MICs were determined by the CLSI M38-A2 broth microdilution methodology of the CaLS Institute (2008). Briefly, stock solutions of either voriconazole (VRZ), AmB, liposomal amphotericin B (AmBisome), or menadione (Mnd) were obtained from Sigma-Aldrich. AmB, Mnd, and VRZ were dissolved in dimethyl sulfoxide. AmBisome was dissolved in sterile water. The antifungal agents were tested over a range of final concentrations (0.015–8 µg/ml for AmB, VRZ, and AmBisome, 0.39–200 µg/ml for MnD). MICs were defined as the lowest concentration of each treatment completely inhibiting fungal growth (observed by light microscopy).

Spot assay

Freshly harvested conidia were serially diluted in DDW to concentrations of 10^7, 10^6, 10^5, and 10^4/ml. 10 µl of conidial dilutions were spotted on AMM or RPMI–MOPS agar plates (with/without xylose where required) in the presence of the specified stress-inducing

agents as indicated. Thermotolerance was tested at 50°C and hypoxic conditions were established at 0.2% (v/v) O_2 and 5% (v/v) CO_2 in an H35 Hypoxystation (Don Whitley Scientific, Bingley, UK). Growth was documented after incubation for 48 or 60 h at 37°C depending on the growth rate.

Ergosterol and sphingolipid analysis by LC–TQ

Ergosterol was separated using the Prominence high performance liquid chromatography system consisting of the controller CBM-20A, autosampler SIL-20AC, column oven CTO-20A, pump LC-20AD, and degasser LC-20A5R (Shimadzu, Duisburg, Germany). Collected biomass was inactivated in 2 ml $HCCl_3$. After addition of 1 ml H_2O, 1 ml methanol and 10 µl 10 mM cholesterol as internal standard (Merck KGaA, Darmstadt, Germany), samples were mixed in a multitube vortexer (VWR, Darmstadt, Germany) for 10 min and subsequently centrifuged for 5 min at 3000 × *g*. The lower $HCCl_3$ phase was transferred into a new glass centrifuge tube. The extraction was repeated with additional 2 ml $HCCl_3$. The combined $HCCl_3$ phases were evaporated and redissolved in 1 ml $HCCl_3$/methanol [1:4 (v/v)]. Triplicates of 10 µl portions were diluted to a final volume of 100 µl in sample vials. 10 µl were applied on a MultoHigh 100 RP18-3 60 × 2 mm column (CS Chromatographie Service GmbH, Langerwehe, Germany) maintained at 35°C. The column was equilibrated with 90% of a 1% aqueous formic acid solution and 10% (v/v) methanol at a flow rate of 400 µl/min. The eluent changed to 100% methanol after injection. The flow rate gradually increased to 800 µl/min between 3 and 5 min. Mass spectrometric determination of ergosterol (m/z 379 > 69) and the internal standard cholesterol (m/z 369 > 161) was performed using the QTrap triple quadrupole mass spectrometer (Sciex, Darmstadt, Germany) run in the multiple reaction monitoring mode using positive atmospheric pressure chemical ionization at 450°C. Data analysis was performed using Analyst 1.6.3 (Sciex). Sphingolipid metabolites were determined as described in Bode and Gräler (2012).

Mouse model of IPA

Six-week-old ICR female mice were supplied by Envigo (Indianapolis, IN, USA). Mice were immunocompromised by two subcutaneous injections with 300 mg/kg cortisone acetate (CA), given 3 days before infection, and on the day of infection (CA model) or injected subcutaneously with cyclophosphamide (CP; 150 mg/kg) and CA (150 mg/kg) 3 days prior to infection, and with CP (150 mg/kg) on the day of infection, 3- and 6-days postinfection (CP model). Mice were housed in sterile cages with sterile bedding and provided with sterile feed and drinking water. The mice were anaesthetized by intraperitoneal injection with 100/10 mg/kg ketamine + xylazine and infected intranasally with 5 × 10^5 conidia of WT, *rtaA*^{C}, and Δ*rtaA* strains, suspended in 20 µl of 0.2% (v/v) Tween 20 in saline solution [0.9% (w/v) NaCl]. Endpoints for sacrifice were defined by a drop of >15% in body weight and/or signs of acute distress. Mice were monitored for 28 days. The study was carried out in accordance with the recommendations of the Ministry of Health (MOH) Animal Welfare Committee, Israel. The protocol was approved by the MOH Animal Welfare Committee, Israel (protocol number MOH 01–17-035).

LC–MS/MS analysis of natural products

Extraction and detection of natural products were carried out as described previously (Stroe et al. 2020). Identification of fumicyclines (also referred to as neosartoricins) was achieved by comparison with the authentic reference neosartoricin (Biomol, Hamburg, Germany).

Fluorescence microscopy

For fluorescence microscopy of filipin and Nile red-stained hyphae, ibidi channel slides (ibidi GmbH, Gräfelfing, Germany) were inoculated with 1 × 10^4 conidia in AMM in the presence or absence of 0.04 or 0.08 µg/ml AmB and incubated overnight at 37°C in a CO_2 incubator. On the next day, the mycelium was fixed for 20 min at room temperature with 3.7% (v/v) formaldehyde/phosphate-buffered saline (PBS) followed by a washing step. Afterwards the samples were stained with 50 µg/ml of the sterol stain filipin-III (Sigma-Aldrich, Taufkirchen, Germany) and 10 µg/ml of the fluorogenic lipid dye Nile red (Sigma-Aldrich) for 10 min at room temperature. After a final washing step, the slides were analysed using a Zeiss LSM 780 confocal laser scanning microscope (Carl Zeiss GmbH, Jena, Germany) and evaluated by a bioinformatic deep learning (DL) approach as described in the following.

A DL-based approach has been employed to identify *A. fumigatus* hyphae using transmitted light (TL) images. To train the DL network, 3D images of *A. fumigatus* WT hyphae labelled with Concanavalin A-FITC were generated using a Zeiss LSM 780 confocal laser scanning microscope (Carl Zeiss GmbH). In parallel, *A. fumigatus* was visualized *via* TL bright field microscopy. Images were acquired as z-stacks with a bit depth of 16. Each image covered an area of 224.92 µm^2 × 224.92 µm^2 at a pixel resolution of 0.109 µm × 0.109 µm. Since the required number of z-layers of the stacks depended on the vertical growth of the hyphae, each stack consisted of the proper number of slices to cover the entire structure, resulting in ∼13–46 slices per z-stack with 0.75 µm axial slice distance. In total, 16 z-stacks of WT samples were provided for training the DL model.

For the intensity-based analysis, 2D images of Nile red-stained intracellular lipid vesicles and filipin-stained ergosterol were recorded alongside the TL images. Three to five images were acquired per sample, each originating from separate, nonoverlapping regions of the sample. The dimensions of each image were 224.92 µm^2 × 224.92 µm^2, capturing details at a resolution of 0.219 µm × 0.219 µm.

The software Huygens Professional (SVI, Hilversum, Holland) was used to correct for chromatic aberration in the 3D images, with an estimated aberration value of zero (for more details about the DL approach see the Supplementary material and below).

For microscopy analysis of the RtaA-GFP^{PXylP} strain, 8-well chamber µ-slides (ibidi GmbH) were inoculated with 1 × 10^3 *A. fumigatus* conidia in AMM containing 1% (w/v) xylose in the presence or absence of 0.04 µg/ml AmB and incubated overnight at 37°C in ambient air. After incubation, the mycelium was either stained with 10 µg/ml Nile red (Sigma-Aldrich) for 10 min at room temperature or with 5 µg/ml FM 4–64 (Thermo Fisher Scientific, Dreieich, Germany) for 10 min on ice. The stained slides were analysed on a Zeiss LSM 780 confocal laser scanning microscope (Carl Zeiss GmbH).

Nucleic acid hybridization

Gene deletion of *rtaA* as well as green fluorescent protein (GFP) and xylose-promoter integration of RtaA-GFP^{PXylP} was verified by Southern hybridization. Briefly, genomic DNA of *A. fumigatus* was extracted from ground mycelium using the MasterPure Complete DNA and RNA purification Kit (Lucigen, LGC group, Teddington, UK) and digested by restriction enzymes as detailed in the Supplementary material. Resulting DNA fragments were

separated by agarose gel electrophoresis and transferred onto Hybond-N+ membranes (GE Healthcare Bio-Sciences, Munich, Germany) by capillary blotting. Gene-specific DNA probes were generated by polymerase chain reaction (PCR), including digoxigenin (DIG)-labelled dUTPs (Jena Bioscience, Jena, Germany). DIG-labelled probes were hybridized in 20 ml hybridization buffer [19 ml 5x SSC, 0.1% (w/v) SDS, 50 g/l dextrane sulfate, and 1 ml Western Blocking Reagent (Roche Diagnostics)] and detected using anti-DIG AP fab fragments (Roche Diagnostics) and CDP-Star as chemiluminescence substrate (Roche Diagnostics). The blot was imaged by an Octoplus QPLEX CCD camera (NH DyeAGNOSTICS, Halle, Germany). Oligonucleotides used for amplifying DNA probes are listed in Table S3.

For northern hybridizations, RNA was isolated from *A. fumigatus* mycelium using the RNeasy Plant Mini Kit (Qiagen, Hilden, Germany). 10 µg of total RNA were separated on a denaturing agarose gel [1.2% (w/v) agarose, 40 mM MOPS, 10 mM sodium acetate, 2 mM EDTA, 2% (v/v) formaldehyde, pH 7)]. Blotting, hybridization, and detection were done as described above. The primers used to generate the DNA probe specific to the 5′ region of the gene *rtaA* are listed in Table S3.

RT-qPCR

For real time quantitative PCR (RT-qPCR) analysis of *rtaA* expression in different *Aspergillus* species, *A. terreus*, *A. lentulus* with low or high AmB MIC as well as *A. fumigatus* WT and *A. fumigatus* RtaA^{PXylP} strains were grown in the presence or absence of 0.125 µg/ml AmB. RNA was extracted from ground mycelium using the Universal RNA Kit (Roboklon, Berlin, Germany) followed by DNase digest utilizing the TURBO DNA-free Kit (Thermo Fisher Scientific). cDNA was synthesized using the RevertAid first strand-cDNA-Synthesis Kit (Thermo Fisher Scientific). All qPCR reactions were carried out on a CFX Duet Real-Time PCR System (BioRad, Feldkirchen) equipped with the CFX Maestro Software 2.3, using the Luna Universal qPCR Master Mix (New England Biolabs, Frankfurt am Main). The *A. fumigatus rtaA* orthologues *ATEG_04110* (*A. terreus*) and *IFM58399_04074* (*A. lentulus*) were used for species-specific primer design. Three biological replicates for every strain used were measured in three technical replicates each. All genes were normalized to the expression of the reference gene β-actin using the $2^{-\Delta\Delta Ct}$ method (Livak and Schmittgen 2001). All RT-qPCR primers had an efficiency between 90% and 110%. Primers for target amplification, as well as their efficiency, are listed in Table S3.

Amino acid alignments and phylogenetic analysis

The amino acid sequence of RtaA (Afu3g12830) was analysed for protein family classification and domain prediction using InterPro (Paysan-Lafosse et al. 2023). Pairwise sequence alignment with *Saccharomyces cerevisiae* RTA1 was performed using EMBOSS Stretcher (Myers and Miller 1988) and transmembrane topology prediction using DeepTMHMM (Hallgren et al. 2022). For phylogenetic analysis of orthologues of Afu3g12830 and all fungal proteins containing RTA1 domain were identified using OrthoMCL release 6.21 (Chen et al. 2006). For the phylogenetic reconstruction of all RTA1 domain-containing fungal proteins, orthogroup sequences were included in the alignment if the orthogroup contained >4 sequences and >97% of the sequences in the orthogroup contained an annotated RTA1 domain (PFAM number PF04479). Amino acid sequences were aligned using MUSCLE v3.8 (Edgar 2004). The resulting alignment was trimmed using ClipKit v2.3.0 (Steenwyk et al. 2020) in smart-gap mode. A maximum-likelihood phylogeny was inferred using IQ-TREE v2.2.0.3 (Minh et al. 2020). ModelFinder in IQ-TREE was used to identify Q.pfam+G4 as the best substitution model for both phylogenies based on Bayesian information criterion. Bootstrapping was performed using 1000 ultrafast bootstraps. The phylogeny was visualized using ggtree 3.11.1 (Yu 2020).

Image data analysis

To identify hyphae based on the TL, a DL segmentation model was trained on pairs of TL images and their corresponding Concanavalin A-stained channel (Fig. S10A). The dataset included 16 z-stack images, totaling 400 2D image slices. Of the 16 z-stacks, 15 3D images (corresponding to 357 2D slices) were used for training and validation. The remaining one z-stack was reserved for model testing and evaluation. Given the challenges of working with a limited dataset in training DL models, data augmentation methods, such as image rotation, flipping, translation, cropping, and blurring were applied (Mikołajczyk and Grochowski 2018, Shorten and Khoshgoftaar 2019). This approach expanded the training dataset to 5712 2D images.

To obtain the hyphal structure masks, several preprocessing steps were applied to the Concanavalin A-stained fungus, including contrast enhancement and noise reduction. Subsequently, the enhanced images were converted into a binary mask (Fig. S10B). For the training and validation stages, the EfficientNetB5-UNet++ model was chosen due to its known efficiency and precision in segmentation tasks (Ronneberger et al. 2015, Zhou et al. 2018, Tan and Le 2019, Lourenço-Silva et al. 2022). The model showed significant accuracy, with a Dice score of 83.08% on the test data (Fig. S10C).

The hyphal masks were generated from the TL channel by the trained DL model (Fig. S10D). Subsequently, the binary masks were used to record the corresponding average intensity values of Nile red and filipin across the entire mask. Moreover, Otsu thresholding was applied to filter out low-intensity values of the foreground pixels, thereby emphasizing regions characterized by higher illumination associated with lipid concentration (Fig. S10E). More details are provided in the Supplementary material.

Statistical analysis

Data and statistical analysis were analysed with the GraphPad Prism 8 software package (GraphPad Software, Inc, San Diego, CA, USA) or the Microsoft Excel software package (Microsoft Corporation, Redmond, WA, USA). The ANOVA test was used for significance testing of two groups. Differences between the groups were considered significant at $P \leq .05$. Mortality results were analysed by the log-rank test for Kaplan–Meyer survival curve, but *t*-test was used for significance testing of two groups. Differences between the groups were considered significant at $P \leq .05$. Statistical analysis for intensity-based image analysis was conducted using SciPy v1.10.1 library in Python v3.10. To compare multiple independent samples, Kruskal–Wallis test with Benjamini–Hochberg adjustment was employed. Significance was defined as a *P*-value $< .05$. Statistical test results were included in the figure legends as follows: $^{*}P < .05$, $^{**}P < .01$, and $^{***}P < .001$. Effect sizes were calculated as Hedges' g, where a value of ∼0.2 indicates a small effect, 0.5 suggests a moderate effect, and 0.8 or higher indicates a large effect.

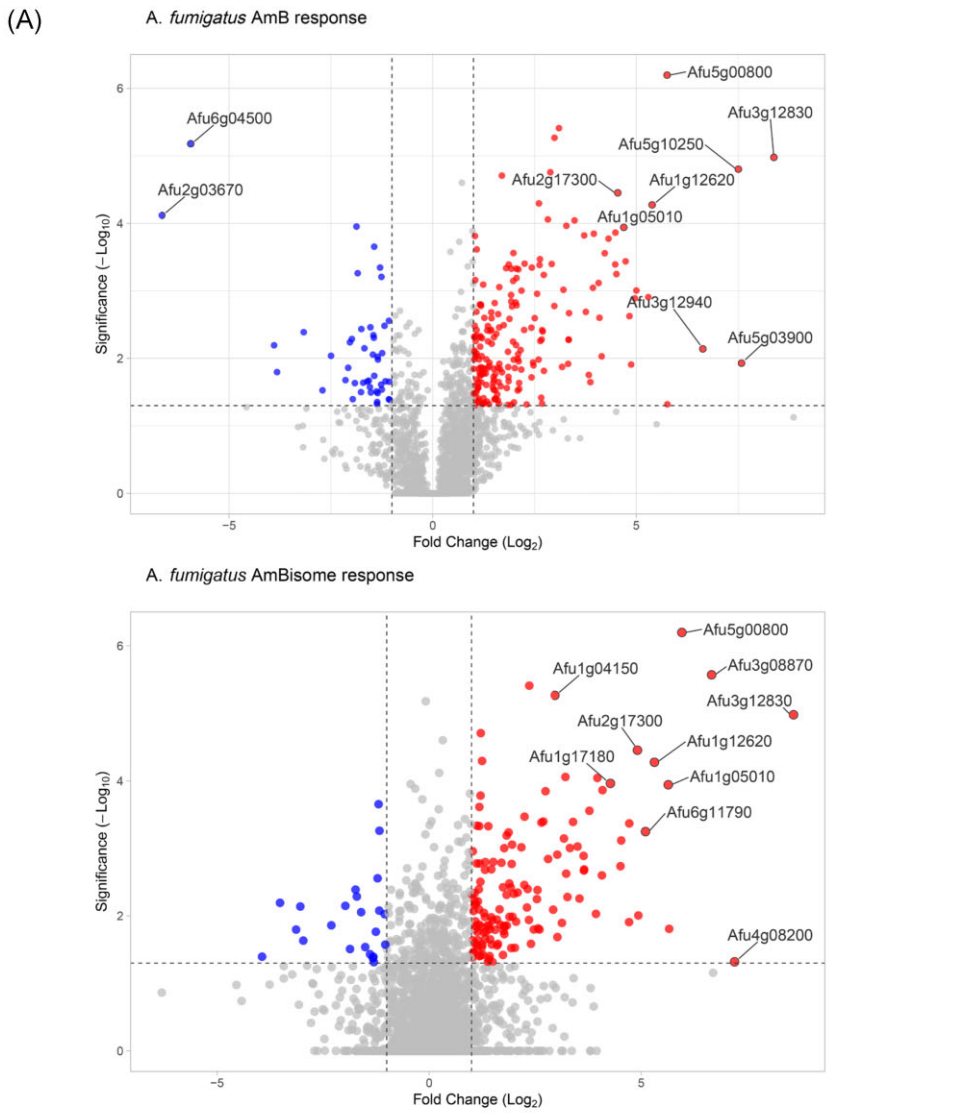

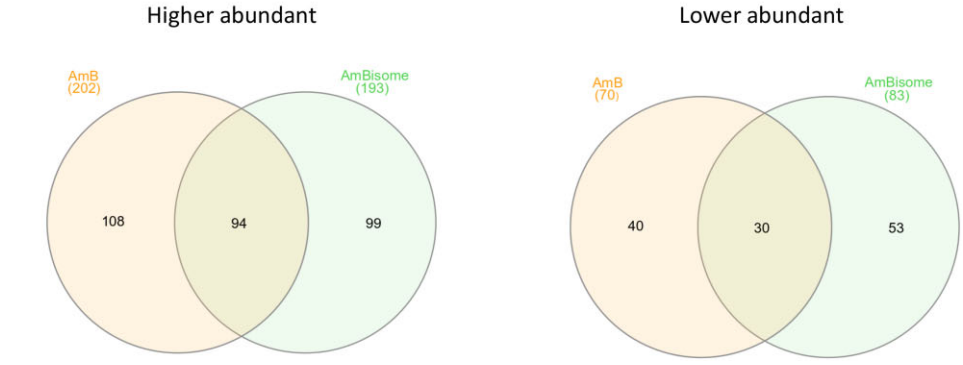

Figure 1. Proteomic changes in *A. fumigatus* after exposure to AmB and liposomal amphotericin B (AmBisome/L-AmB). (A) Volcano plots showing expression values for *A. fumigatus* after exposure for 4 h to AmB and AmBisome (L-AmB). The *x*-axis shows the log2-fold change, while the *y*-axis shows the −log10 transformed *P*-value. (B) Venn diagram of the proteomic response of *A. fumigatus* to AmB and AmBisome.

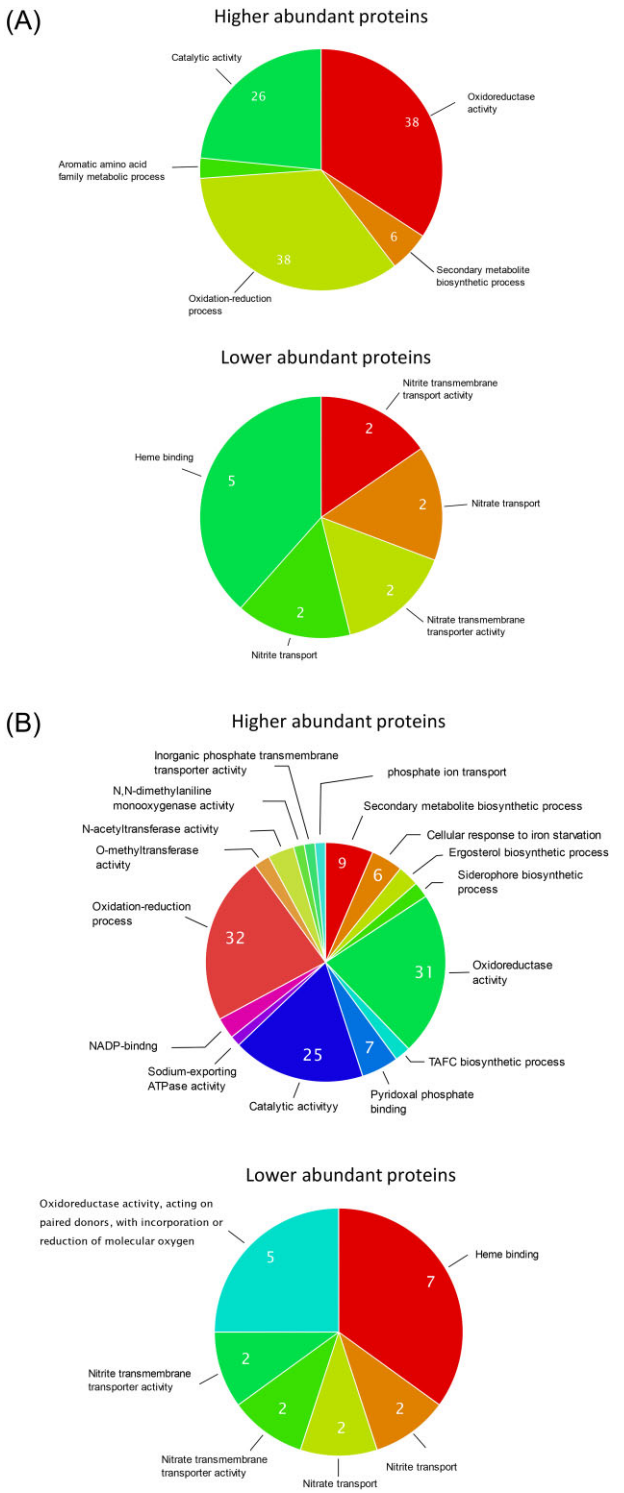

Figure 2. PSEA using GO terms to detect differences in the response of *A. fumigatus* to (A) AmB and (B) AmBisome (L-AmB). Proteins with an abundance change of >2- or <0.5-fold were included in the analysis by the web tool FungiFun 2 (https://elbe.hki-jena.de/fungifun/). Enriched GO terms for proteins with increased (2-fold) and decreased (−2-fold) abundances are shown. (C) Detection of fumicycline A and fumicycline C by LC–MS in cultures of *A. fumigatus* exposed to AmB. Extracted-ion chromatograms (EIC) for (left) fumicycline A (m/z 423.5 $[M-H]^-$), (middle) fumicycline B (m/z 441.5 $[M-H]^-$), and (right) fumicycline C (m/z 483.5 $[M-H]^-$) from LC–MS analysis of *A. fumigatus* culture with DMSO as control (top) or AmB (middle) are shown. The neosartoricin B and neosartoricin C standards are shown at the bottom with the same EIC as fumicycline B and C, respectively.

Results

Proteomic analysis of *A. fumigatus* response to AmB and AmBisome

To gain a better understanding of the proteomic response of *A. fumigatus* to AmB and its liposomal formulation AmBisome, we first determined a suitable, sublethal concentration for both antifungals, which induced a robust growth inhibition, but did not lead to a complete growth arrest. Therefore, growth curves of *A. fumigatus* cultures treated with different concentrations of AmB and AmBisome in comparison to Dimethyl sulfoxide (DMSO) controls were measured, using backscattered light detection. Based on the results, for subsequent proteomic analyses concentrations of 0.125 µg/ml AmB and 7 µg/ml AmBisome were selected, which met the criteria (Fig. S4). To further investigate the proteomic response of *A. fumigatus* to AmB, we conducted additional experiments in which we exposed the fungus to 0.125 mg/l AmB for different time intervals and analysed the resulting proteomic changes. Specifically, we performed three technical replicates each at time points of 1, 2, and 4 h and set a threshold of ≥4-fold due to the limited number of replicates. The 4-h exposure time resulted in the highest number of proteins (97 out of 3604 proteins) with significant changes in abundance, whereas only a small number of proteins showed exclusively significant changes after 1 and 2 h of AmB exposure, but not at 4 h. (Fig. S5). For this reason, we investigated the proteomic response of *A. fumigatus* to AmB and AmBisome after 4 h exposure. The LC–MS/MS-based proteomic analyses identified a total of 3680, 3683, and 3448 different proteins in the AmB-treated, AmBisome-treated, and untreated *A. fumigatus* samples, respectively (proteins present in at least two out of three biological replicates). We observed increased levels of numerous *A. fumigatus* proteins (≥2-fold) in response to AmB, including 202 and 193 proteins upon AmB and AmBisome exposure, respectively (Fig. 1A, Table S7). The level of 94 proteins increased significantly under both conditions in comparison to untreated *A. fumigatus* cultures (Fig. 1B, Table S7). In contrast, the number of proteins showing reduced abundance in response to antifungal exposure was considerably smaller, with 70 for AmB and 83 for AmBisome, and an overlap of 30 proteins for both drug formulations (Fig. 1A and B, Table S7).

Protein set enrichment analysis (PSEA) indicated that enzymes involved in oxidation–reduction processes, secondary metabolite biosynthesis, and aromatic amino acid metabolism were significantly enriched upon exposure to AmB, whereas nitrate transport and nitrate reduction activity were notably decreased (Fig. 2A). The addition of AmBisome resulted in a similar proteomic response compared to that of AmB. However, in contrast to AmB, the addition of AmBisome also resulted in an enrichment of proteins involved in the response to iron starvation and ergosterol biosynthesis (Afu2g00320, Erg3) among the proteins with increased abundance (Fig. 2B, Table S6). Interestingly, the level of reactive oxygen species (ROS)-detoxifying enzymes did not increase under both conditions with the exception of a predicted glutathione S-transferase Afu2g17300. Catalase CatB even decreased in abundance by 1.5–2-fold in response to both amphotericin formulations.

The PSEA data revealed that AmB and AmBisome induce the production of secondary metabolites in *A. fumigatus* (Table S6). The level of four out of six proteins (FccB, FccC, FccA, and FccD) encoded by the fumicycline gene cluster, significantly increased by a factor of 3–23-fold after AmB and AmBisome exposure (Table S6). The induction of fumicycline production by AmB was also verified at the metabolome level by LC–MS/MS analysis (Fig. 2C). Notably,

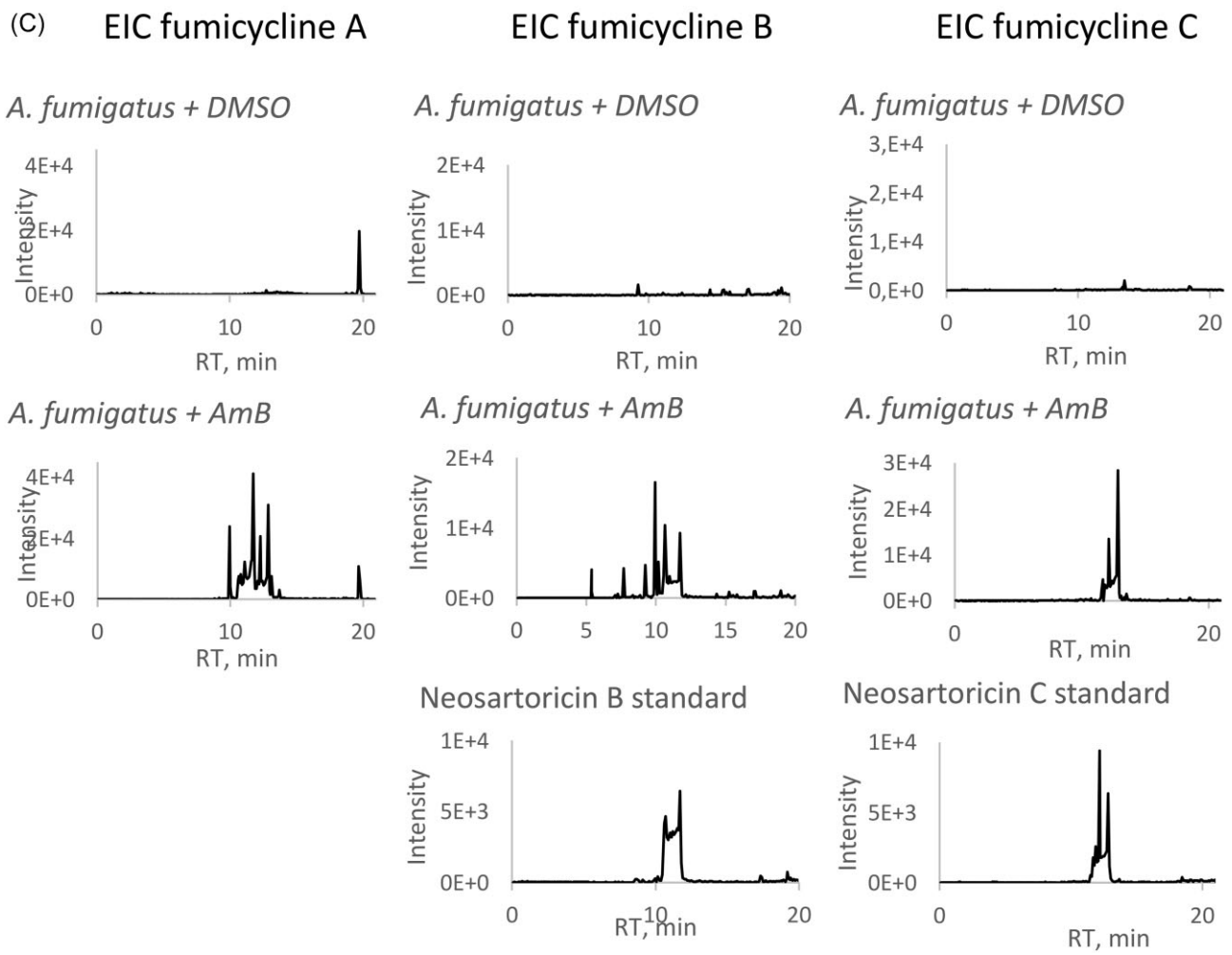

Figure 2. *Continued.*

the fumicycline gene cluster of *A. fumigatus* is known to be induced by interaction with the Gram-positive soil bacterium *Streptomyces rapamycinicus* (König et al. 2013). Likewise, the expression of enzymes involved in the biosynthesis of the copper-binding isocyanide xanthocillin (XanA, XanB, XanE, XanF, and XanG) and the iron(III)-chelating complex HAS (HasB, HasC, and HasH) was found to be significantly upregulated (Table S6) (Yin et al. 2013, Lim et al. 2018). Collectively, these findings showed that the antifungal AmB derived from the secondary metabolite produced by *S. nodosus* triggers the activation of secondary metabolite biosynthesis gene clusters in *A. fumigatus*.

Conversely, exposure to AmB and AmBisome resulted in a significant decrease in the levels of Pyr6 (Afu6g13980) and Pyr1 (Afu6g13920), which are enzymes involved in the biosynthesis of the secondary metabolite pyripyropene A (Itoh et al. 2010) (Table S7). The AMP-activated protein kinase Afu6g04500, which is part of the Snf1-complex involved in regulating adaptation to glucose limitation in *S. cerevisiae*, was also found to have significantly decreased in abundance (Shashkova et al. 2015).

Among the 14 proteins with the highest increase in abundance following exposure to AmB and AmBisome, it is evident that several secondary metabolite biosynthesis enzymes were included, such as the xanthocillin biosynthesis enzymes XanB and XanE, as well as the alcohol dehydrogenase Afu5g10220, which is part of an uncharacterized NRP-like cluster (Table 1, Table S7). In addition to secondary metabolite biosynthesis enzymes, the list of the top 14 most abundant proteins included membrane transporters (Afu1g05010/Mfs56, Afu1g12620, and Afu6g03690/Ena1) and a putative glycosylphosphatidylinositol (GPI) transamidase responsible for attaching GPI-anchors to proteins (Afu4g08200/PIG-U). The corresponding orthologous gene *GAB1* has been demonstrated to be essential in *S. cerevisiae* (Grimme et al. 2004). Moreover, the list of the top 14 most abundant proteins also includes a putative antimicrobial peptide (Afu8g00710), the aforementioned glutathione S-transferase (Afu2g17300), which is generally involved in detoxification of ROS and xenobiotics, and several uncharacterized proteins (Afu4g09230, Afu5g00800, and Afu6g11790). The gene *hppD*, which encodes the enzyme 4-hydroxyphenylpyruvate dehydrogenase (Afu2g04200), is part of a gene cluster (*Afu2g04200–Afu2g04262*) known to be involved in the degradation of tyrosine (Schmaler-Ripcke et al. 2009). Additionally, the enzymes HmgA, FahA, and MaiA, which are further involved in this degradation pathway, were also activated 3.6–10.1-fold after AmB treatment (Table S7). A remarkably substantial increase in abundance of more than 300-fold was observed for an RTA-like protein encoded by the gene *Afu3g12830* after AmB or AmBisome exposure and designated here as RtaA. To investigate the possible involvement of these proteins in AmB resistance, we selected nine proteins for further analysis (Table 1, in bold) and generated knockout

Table 1. Top 14 AmB-upregulated proteins identified by proteomic analysis. Genes in bold were deleted in *A. fumigatus*.

Number	Gene ID	+AmB (-fold)	+AmBisome (-fold)	Description
1	***Afu3g12830***	332.3	385.3	RTA1 domain protein
2	*Afu4g08200*	54.3	147.0	GPI transamidase component PIG-U involved in transfer of GPI to proteins
3	***Afu5g00800***	54.1	62.0	Conserved hypothetical protein (crystallins superfamily)
4	***Afu1g12620***	41.9	39.6	Putative toxin efflux pump
5	*Afu2g04200*	39.2	8.1	4-Hydroxyphenylpyruvate dioxygenase (HppD) involved in L-tyrosine degradation
6	***Afu5g02660***	32.0	10.0	Isocyanide synthase-dioxygenase XanB
7	***Afu5g02640***	31.2	12.5	O-methyltransferase XanE
8	***Afu8g00710***	29.3	26.2	Secreted antimicrobial peptide, putative
9	*Afu5g10220*	28.5	9.4	Alcohol dehydrogenase, zinc-containing, putative
10	***Afu1g05010***	25.9	49.8	Putative MFS transporter Mfs56
11	*Afu2g17300*	23.3	30.1	Predicted glutathione S-transferase
12	***Afu6g11790***	22.8	34.2	Conserved hypothetical protein
13	***Afu4g09230***	22.4	17.0	Conserved hypothetical protein
14	*Afu6g03690*	22.3	10.5	Putative P-type ATPase sodium pump Ena1

Table 2. MIC values of AmB, AmBisome, VRZ, and Mnd in WT and mutant strains.

Strains	AmB (μg/μl)	AmBisome (μg/ml)	VRZ (μg/ml)	Mnd (μg/μl)
WT	0.5	0.125	0.5	31.25
Δ*Afu3g12830* (Δ*rtaA*)	0.125	0.03	0.5	31.25
rtaA^{C}	0.5	0.125	0.5	31.25
Δ*Afu5g00800*	0.5	0.125	0.5	31.25
Δ*Afu1g12620*	0.5	0.125	0.5	31.25
Δ*Afu5g02660*	0.5	0.125	0.5	31.25
Δ*Afu5g02640*	0.5	0.125	0.5	31.25
Δ*Afu8g00710*	0.5	0.125	0.5	31.25
Δ*Afu1g05010*	0.5	0.125	0.5	31.25
Δ*Afu6g11790*	0.5	0.125	0.5	31.25
Δ*Afu4g09230*	0.5	0.125	0.5	31.25

mutant strains of the corresponding genes (for more details see the Supplementary material).

The Δ*rtaA* mutant strain is more sensitive to AmB and AmBisome

To assess the susceptibility of the deletion strains to AmB and AmBisome, we conducted an initial evaluation in comparison to VRZ and Mnd controls using the CLSI M38-A2 broth microdilution methodology of the CaLS Institute (2008). Table 2 presents the MIC values in μg/ml of AmB, AmBisome, VRZ, and Mnd after 48 h of incubation at 37°C in RPMI–MOPS medium for both the WT strain and the deletion mutants. The results show that only the Δ*Afu3g12830* (Δ*rtaA*) mutant strain exhibited a 4-fold increased sensitivity to AmB and AmBisome, with MIC values of 0.125 μg/ml and 0.03 μg/ml, respectively, compared to 0.5 μg/ml and 0.125 μg/ml for the WT strain. The complemented *rtaA* null mutant (*rtaA*^{C}) exhibited WT MICs for AmB and AmBisome, indicating that the reintroduction of the *rtaA* gene restored the WT phenotype. We further assessed the susceptibility of these strains to AmB by point inoculation after 60 h of incubation at 37°C in AMM agar (Fig. 3). In agreement with the broth microdilution results, Δ*rtaA* exhibited increased AmB susceptibility compared to the parental and reconstituted *rtaA*^{c} strains. These findings suggest that RtaA contributes to the *A. fumigatus* stress response to AmB and its absence leads to AmB hypersensitivity. In contrast, RtaA has no effect on the sensitivity of the fungus to other antifungal agents tested here. To further characterize the role of RtaA in *A. fumigatus*, we assessed the growth of the Δ*rtaA* strain under various stress conditions, compared to the WT and the *rtaA*^{c}-complemented strain (Fig. 4). For this purpose, the effects of cell wall- (Congo red, calcoflour white, caspofungin, and tunicamycin) and membrane-interfering compounds [SDS, phytosphingosine, α-tomatin, miltefosine, and itraconazole (ITZ)], and of oxidative stress (4 mM H_2O_2), hypoxia [0.2% (v/v) O_2], alkaline growth conditions (pH 8.0), heat (50°C), osmotic stress (1 M NaCl), iron depletion (-Fe plus 0.2 mM BPS), and reductive stress (10 mM DTT) were monitored. We did not observe any differences in growth between the Δ*rtaA* and the WT strain under any of these conditions. However, a 2-fold increase in susceptibility to the polyene antifungal agent nystatin was visible for the Δ*rtaA* strain (MIC of 0.8 μg/ml) compared to the WT (MIC of 1.6 μg/ml), indicating that RtaA specifically protects *A. fumigatus* to some extent against polyene antifungals such as AmB, AmBisome, and nystatin.

The protein sequence of *A. fumigatus* RtaA contains seven transmembrane domains and shows sequence similarity to the *S. cerevisiae* protein Rta1

RtaA belongs to the RTA-like protein family (PF04479/IPR007568), which consists of fungal proteins with multiple transmembrane domains. Some members of this protein family are known to provide resistance against toxic compounds and are also

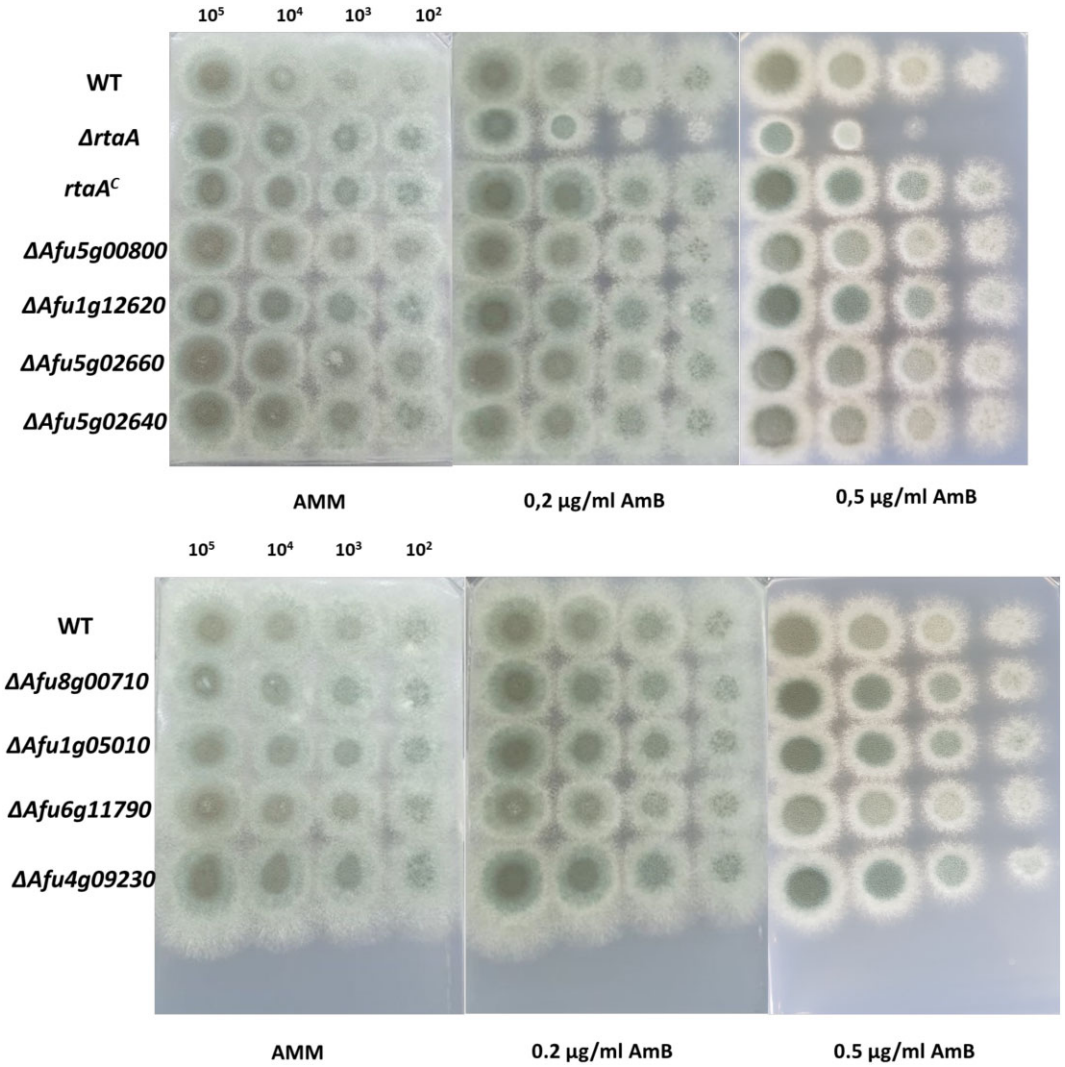

Figure 3. Analysis of mutant strains for AmB sensitivity by point inoculation. The parental WT strain, the deletion strains, and complemented *rtaA*^{C} were point-inoculated on AMM agar plates with increasing concentrations of AmB (0–0.5 µg/µl) for 48 h at 37°C. Each droplet column (from left to right) contained 10^5, 10^4, 10^3, or 10^2 conidia per 10-µl droplet.

designated as fungal lipid-translocating exporter proteins (Manente and Ghislain 2009). To compare RtaA with another RTA-like protein, we performed a pairwise sequence alignment with the *S. cerevisiae* protein Rta1p/YGR213C using EMBOSS Stretcher (Fig. 5A). Rta1p is known to confer resistance against 7-aminocholesterol (Soustre et al. 1996). Our results showed that RtaA shared 42.4% sequence similarity with Rta1p, with an identity of 29.1%, and that both proteins contained seven transmembrane domains. The paralogous *S. cerevisiae* protein YLR06C also exhibited equal sequence similarity with the RtaA protein of *A. fumigatus*. Interestingly, the *A. fumigatus* genome encodes 23 different members of the RTA-like protein family (InterPro entry IPR007568; https://www.ebi.ac.uk/interpro/) highlighting the potential importance of this protein family for the physiology and adaptation ability of this fungus (Fig. S6). Nevertheless, none of the other 22 different RTA-like proteins of *A. fumigatus* was among the 4329 proteins identified in our study, which suggests that they are mainly produced under specific stress or growth conditions.

To investigate the evolutionary relationship of RtaA, we identified 176 orthologues that were present in the Ascomycota subphylum Pezizomycotina and the classes Eurotiomycetes, Sordariomycetes and Dothiomycetes, including some of the most important human- or plant-pathogenic fungi. Phylogenetic analysis revealed that RtaA has the closest similarity to orthologues of other Aspergillaceae, namely many *Aspergillus* species and *Penicilliopsis zonata* (Fig. 5B; Supplementary data). No sequences from the Saccharomycetes class were among the identified orthologues, indicating that *S. cerevisiae* Rta1 is not an orthologue of the RtaA protein. To analyse the phylogenetic relationships of all 23 RTA-like proteins of *A. fumigatus*, we constructed a phylogenetic tree from more than 2500 RTA-like domain-containing sequences in fungi (Fig. S6; Supplementary data). This tree clearly showed that *S. cerevisiae* Rta1 and *A. fumigatus* RtaA are only distantly related to each other and that the RTA-like protein Afu6g09550 is the most closely related *A. fumigatus* protein to Rta1.

RtaA localizes primarily to the cytoplasmic membrane

To investigate the cellular distribution of RtaA–GFP, we generated an *A. fumigatus* strain, which expresses an RtaA–GFP fusion protein under the control of the xylose-inducible *xylP*-promoter *PXylP* in the Δ*rtaA* background. Previous attempts with the native *rtaA* promoter resulted in strains exhibiting only weak GFP signals,

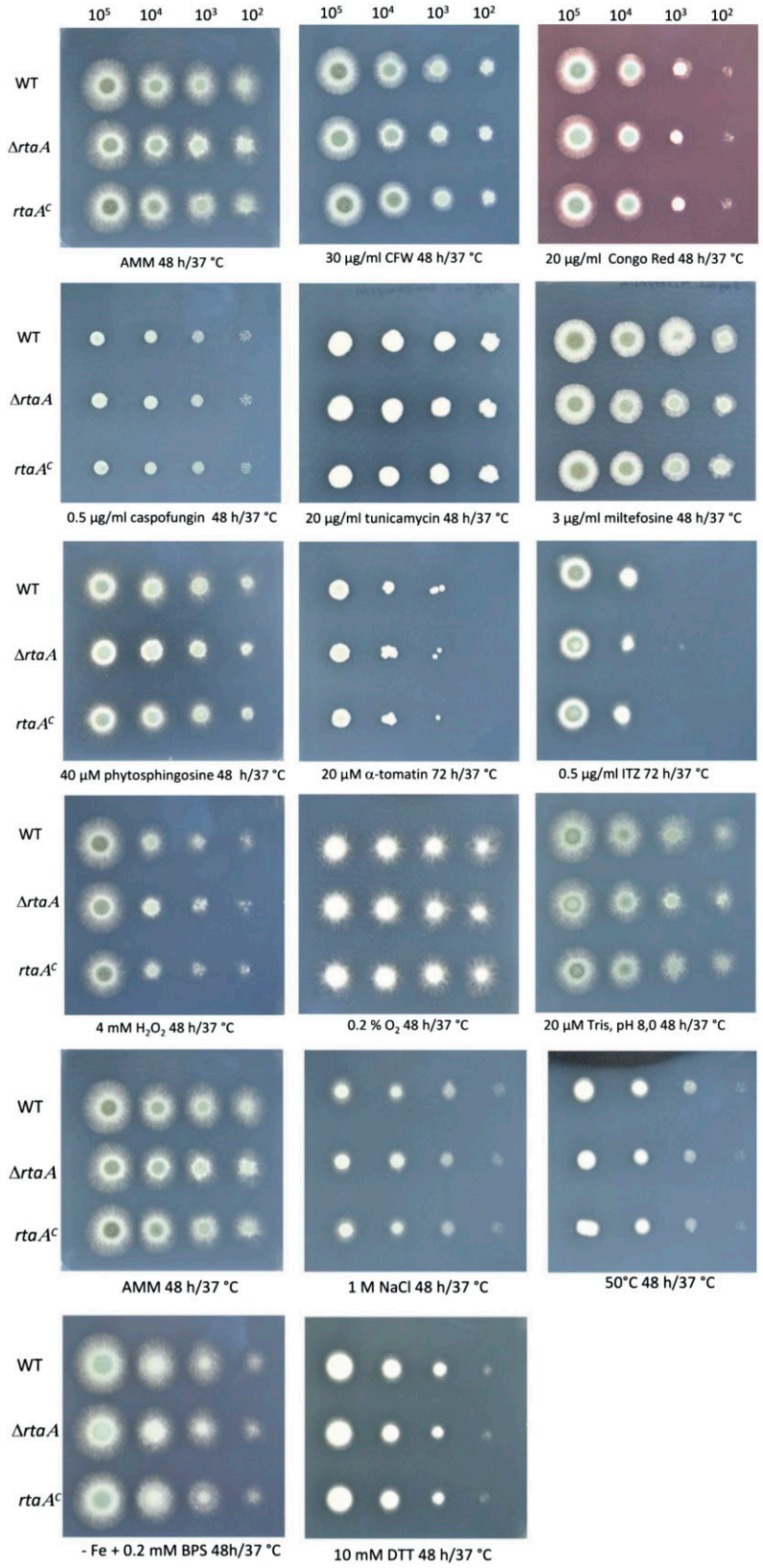

Figure 4. Growth analysis of the *rtaA* deletion mutant. Conidia of *A. fumigatus* strains WT, Δ*rtaA*, and *rtaA*^{C} were spotted on AMM agar plates at a 10-fold serial dilution and tested under different growth conditions for 2–3 days at 37°C, as indicated.

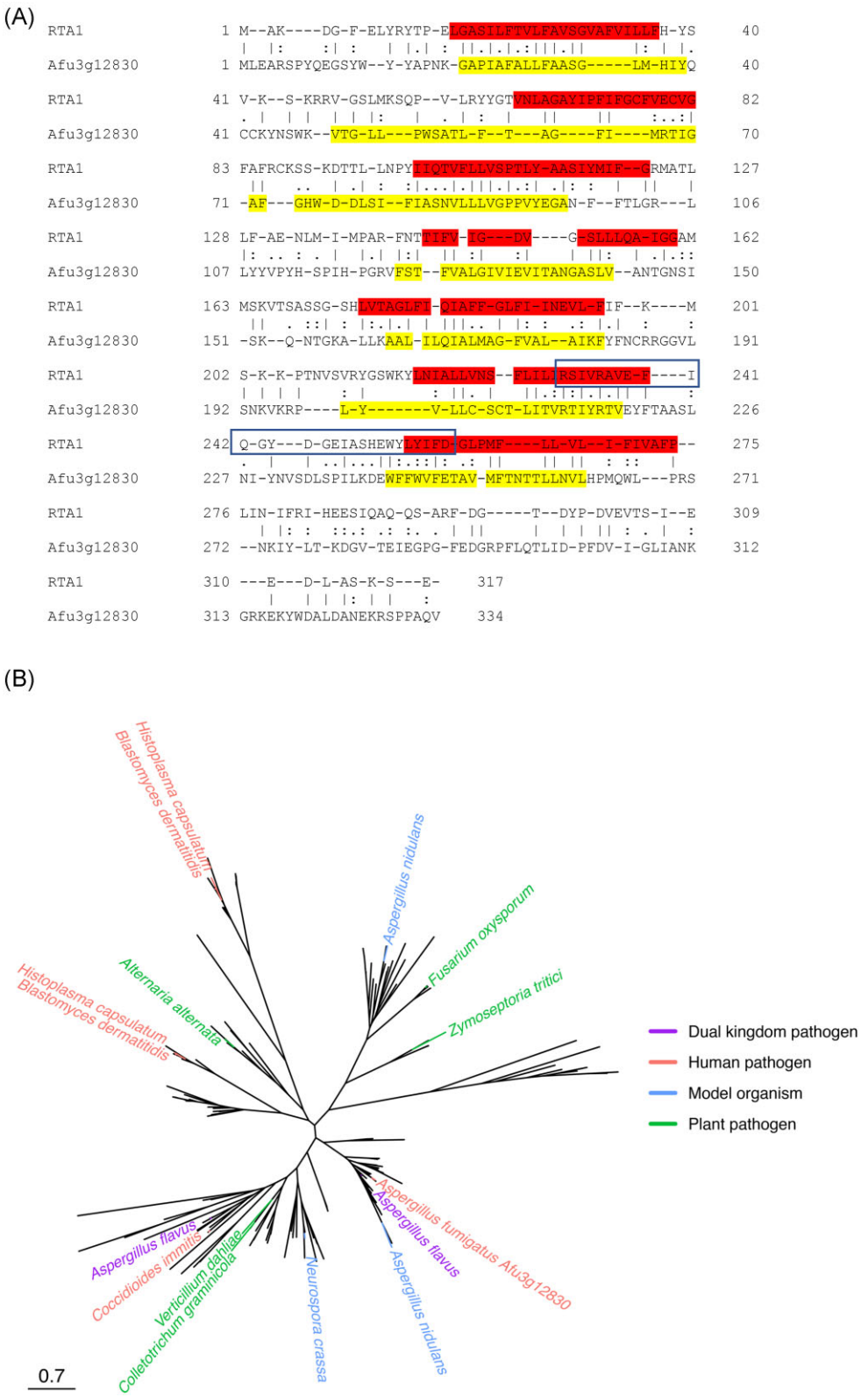

Figure 5. Sequence similarity of *A. fumigatus* RtaA to homologous proteins of other fungal species and cellular localization. (A) Pairwise alignment of the *A. fumigatus* protein RtaA (Afu3g12830) with the protein Rta1 (YGR213C) of *S. cerevisiae* using Strecher EMBOSS (identity 29.1%, similarity 42.4%, and score 521). Predicted transmembrane helices are highlighted. The framedarea represents the postulated Rta1 family signature. (B) The maximum-likelihood phylogeny of fungal Rta1 amino acid sequences. Orthologs from selected human pathogens, phytopathogens, and model organisms are highlighted. See the Supplement material for tree and alignment file. (C) RtaA is localized in membranes. Hyphae of *A. fumigatus* strain RtaA-GFP^{PXylP} were grown in AMM medium containing 1% xylose. Visualization was carried out by confocal laser imaging of the GFP signal alone, with the endosome dye FM4-64 as well as Nile red staining (detection of lipid droplets).

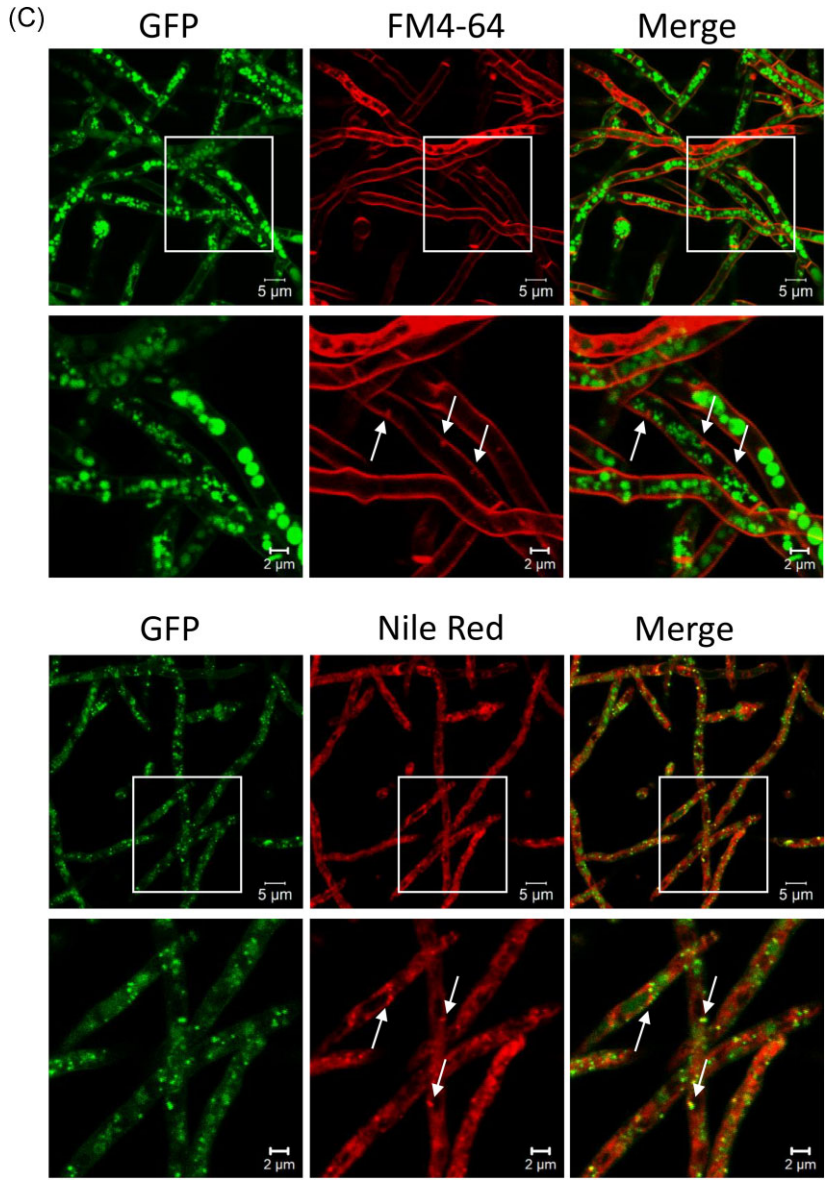

Figure 5. *Continued.*

even with the addition of sublethal concentrations of AmB (data not shown). During hyphal growth, the RtaA–GFP fusion protein, whose production was induced by xylose in the medium, was visible at the cell periphery of hyphae and septa and in larger roundish structures. There were occasional colocalizations of the GFP-signal with Nile red-stained lipid droplets (indicated by arrows in Fig. 5C). However, there was no observable colocalization with FM4-64-stained endosomes (Fig. 5C, arrows show specific endosomes), what speaks against the involvement of RtaA in endocytic membrane transport processes. The addition of 0.04 µg/ml AmB did not have a significant impact on the distribution of RtaA (Fig. S7). These data confirmed the cytoplasmic membrane localization of RtaA, but also indicate a partial accumulation around structures that represent lipid droplets (Fig. 5C).

Inducible overexpression of *rtaA* results in AmB resistance

To investigate the effect of *rtaA* overexpression on the susceptibility of respective strains on antifungal drugs, we generated an *rtaA*-inducible strain of *A. fumigatus* using the xylose-inducible promoter *PXylP*. RtaA expression levels were verified by RT-qPCR. The expression of *rtaA* was significantly higher in the RtaA^{PXylP} strain after the addition of xylose to the medium in comparison to the AmB-induced expression of *rtaA* in the WT (Fig. S2C). Additional supplementation with AmB led to expression levels comparable to the *rtaA* expression level in the WT exposed to AmB (Fig. S2C). After 48 h of incubation at 37°C in RPMI–MOPS medium with or without xylose, we determined the MIC values (µg/ml) of AmB, AmBisome, VRZ, and Mnd for the RtaA^{PXylP} strain, the Δ*rtaA* strain, and the WT strain. The results are summarized in Fig. 6(C). Overexpression of *rtaA* in the presence of 0.5% (w/v) xylose resulted in a 2-fold increase in MIC to AmB and AmBisome (MIC values 1 µg/ml and 0.25 µg/ml, respectively) compared to the parental strain (0.5 µg/ml and 0.125 µg/ml, respectively), with no alteration in sensitivity to VRZ and Mnd. Consistent with our expectations, RtaA^{PXylP} behaved similarly to Δ*rtaA* in the absence of xylose.

To further assess the susceptibility of the strains to AmB, point inoculation assays were performed as described before, and the

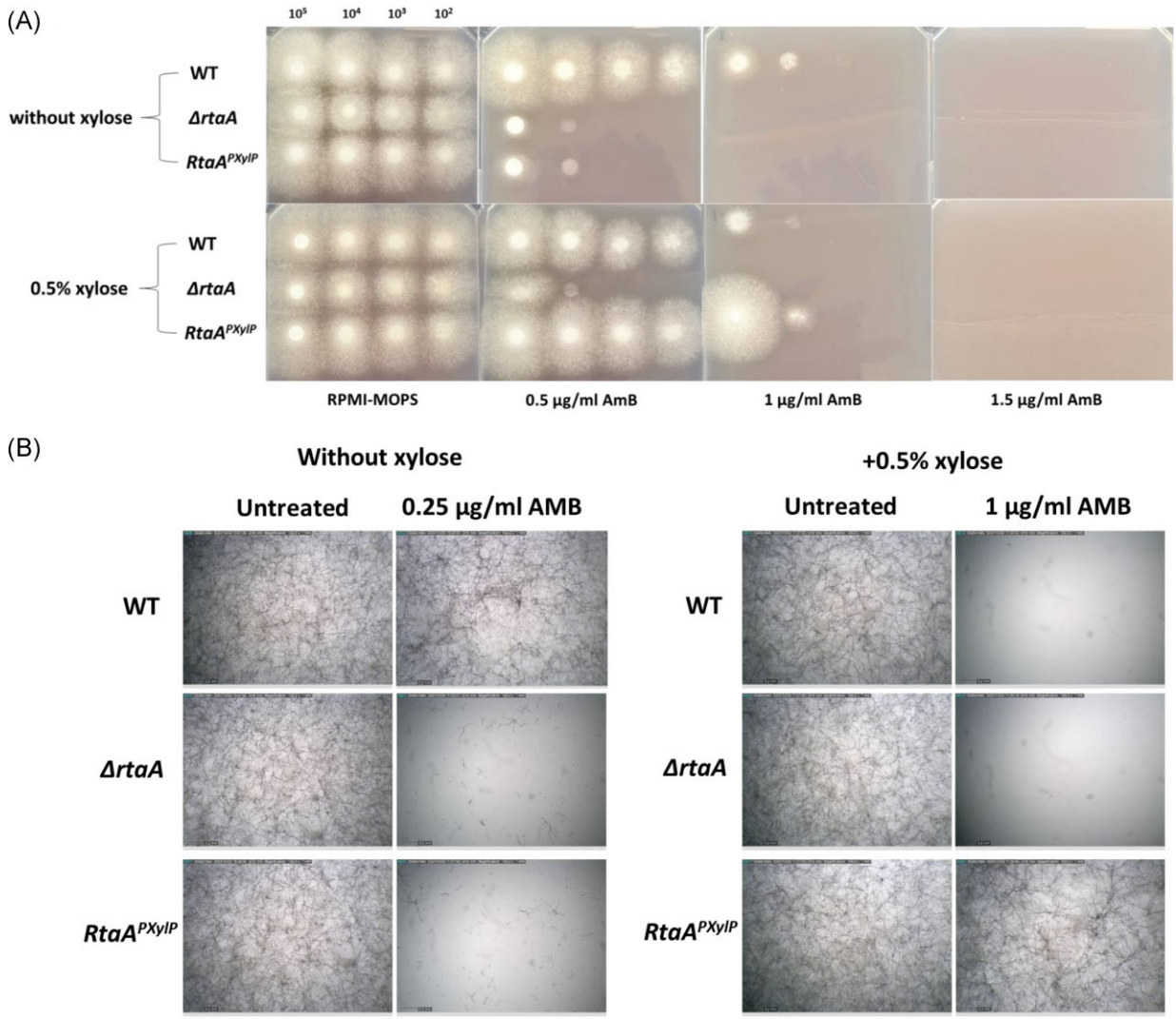

(C)

MIC values of RtaA^{PXylP} in RPMI-MOPS medium

RPMI-MOPS	Strains	AmB (µg/ml)	AmBisome (µg/ml)	VRZ (µg/ml)	MnD (µg/ml)
	WT	0.5	0.125	0.5	31.25
-xylose	Δ*rtaA*	0.125	0.03	0.5	31.25
	RtaA^{PXylP}	0.125	0.03	0.5	31.25
	WT	0.5	0.125	0.5	31.25
+0.5% xylose	Δ*rtaA*	0.125	0.03	0.5	31.25
	RtaA^{PXylP}	1	0.25	0.5	31.25

Figure 6. Reduced AmB susceptibility of *A. fumigatus* overexpressing *rtaA*. (A) Spot assay on RPMI–MOPS agar plates with increasing concentrations of AmB (0–1.5 µg/ml) and with (lower)/without (upper) 0.5% (w/v) xylose added to the medium for 60 h at 37°C. Each droplet column (from left to right) contained 10^5, 10^4, 10^3, or 10^2 conidia per 10-µl droplet. (B) Microscopic analysis of growth in AMM without (left) or with (right) 0.5% (w/v) xylose added to the medium. Images were taken after incubation for 48 h at 37°C.

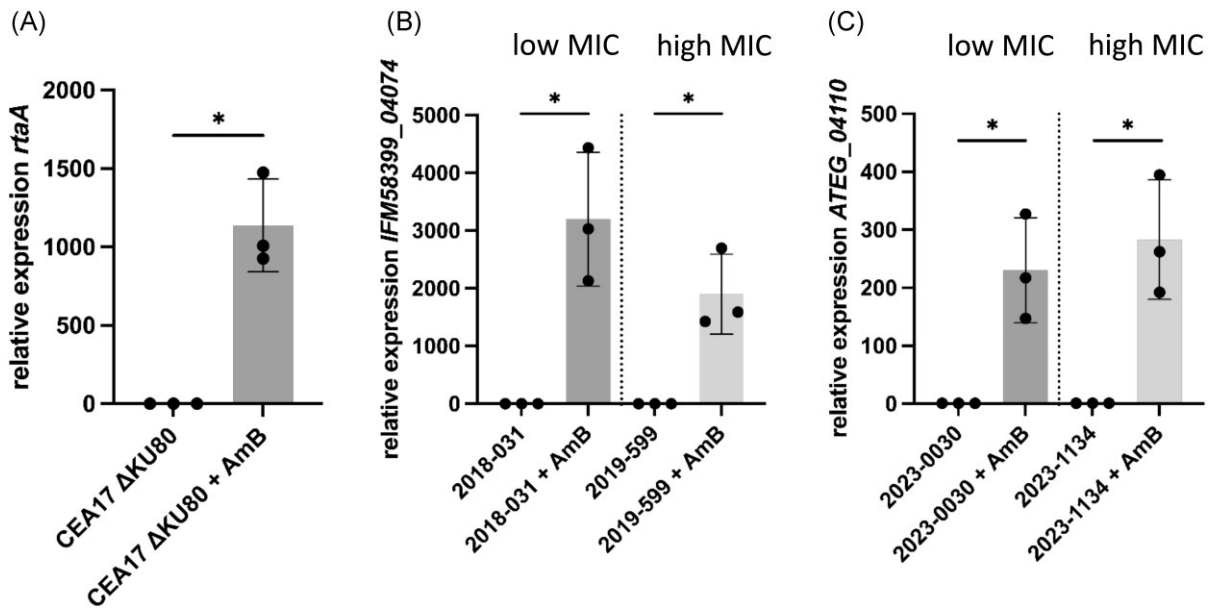

Figure 7. The expression of *rtaA* and *rtaA* orthologues is induced by AmB in different *Aspergillus* species. (A) Expression of *rtaA* in *A. fumigatus* (strain CEA17 Δ*KU80*) is induced by sublethal AmB concentrations. (B) Expression of *IFM58399_04 074*, an *rtaA* orthologue, in two *A. lentulus* strains with low and high MIC of AmB is induced by sublethal concentrations of AmB. (C) Expression of *ATEG_04 110*, an *rtaA* orthologue, in two *A. terreus* strains with low and high MIC of AmB is induced by sublethal concentrations of AmB. The *rtaA* expression levels of not AmB-induced cultures served as controls in (A), (B), and (C). Expression levels of *rtaA* and orthologues were normalized on the expression of *β*-actin and analysed by using the $2^{(-\Delta\Delta Ct)}$ method.

results are presented in Fig. 6. After 60 h of incubation at 37°C in RPMI–MOPS medium with/without xylose, the susceptibility of $RtaA^{PXylP}$ was compared to that of Δ*rtaA* and the WT strain in both solid (Fig. 6A) and liquid (Fig. 6B) media. Notably, the overexpression of *rtaA* in the presence of 0.5% (w/v) xylose resulted in an increased resistance to AmB in the $RtaA^{PXylP}$ strain, as compared to the parental strain. As expected, in the absence of xylose, the AmB susceptibility of strain $RtaA^{PXylP}$ was similar to that of Δ*rtaA*. These findings provide further evidence that the overexpression of *rtaA* confers modest AmB resistance in *A. fumigatus*.

The expression of *rtaA* orthologues in the *Aspergillus* species *A. terreus* and *A. lentulus* is also activated by AmB

To determine if other *Aspergillus* species with more frequently observed AmB resistance also induce the expression of *rtaA* orthologues upon AmB treatment, we quantified the expression levels of the *rtaA* orthologues *ATEG_04 110* (*A. terreus*) and *IFM58399_04 074* (*A. lentulus*) via RT-qPCR in patient isolates of *A. terreus* and *A. lentulus* (Fig. 7). We used both susceptible strains with low AmB MIC and strains with elevated AmB MICs. In all strains, independent of the AmB susceptibility exhibited a significantly higher levels of the respective *rtaA* orthologue when treated with 0.125 µg/ml AmB as compared to untreated controls of the different strains. The highest change in abundance was observed in the *A. lentulus* strains (Fig. 7B). The fold change was comparable to the fold change seen in *A. fumigatus* (Fig. 7A). This indicates that closely related *Aspergillus* species like *A. lentulus* utilize similar mechanisms in the response to AmB, and even the more distantly related *Aspergillus* species *A. terreus* showed a similar regulation pattern. No significant difference in the expression of *rtaA* was determined between susceptible and resistant strains.

rtaA expression is specifically induced by exposure to AmB and nystatin

As described above, the spotting assays conducted with the Δ*rtaA* mutant demonstrated that RtaA confers resistance to AmB while exhibiting no resistance to other clinically significant antifungal agents. To corroborate these observations, we investigated the induction of *rtaA* gene expression by sublethal concentrations of AmB, ITZ, and caspofungin using northern blot analysis. (Fig. 8). Under standard growth conditions in AMM (control, Ctrl), the expression of *rtaA* transcript was below the detection limit. However, exposure to sublethal concentrations of AmB (0.125 µg/ml) for 4 h resulted in a significant increase in the expression of *rtaA*, while no changes in the expression levels of *rtaA* were observed when exposed to sublethal concentrations of ITZ (0.25 µg/ml) or caspofungin (0.1 µg/ml) (Fig. 8A). We also tested two other antifungal polyene macrolides, namely natamycin (2 µg/ml) and nystatin (0.25 µg/ml), of which only nystatin induced the expression of *rtaA*. As a control, we determined the expression of *rtaA* in *A. fumigatus* upon exposure to the antibacterial macrolide erythromycin (64 µg/ml), the polyene antibiotic linearmycin (8 µg/ml), and the ROS-inducing compound Mnd (2 µg/ml). None of these three compounds led to an increased expression of *rtaA* (Fig. 8B). This finding confirms that RtaA specifically mediates resistance to AmB and the structurally similar glycosylated polyene macrolide nystatin and that its expression is induced by sublethal concentrations of these two antifungal drugs, which are both produced by *Streptomyces* bacteria.

Deletion of *rtaA* alters modestly the lipid content of fungal hyphae

Lipid flippases are membrane proteins that play a crucial role in maintaining the lipid asymmetry of cellular membranes by selectively translocating specific lipids between the two membrane leaflets. This lipid asymmetry is critical for a wide range of

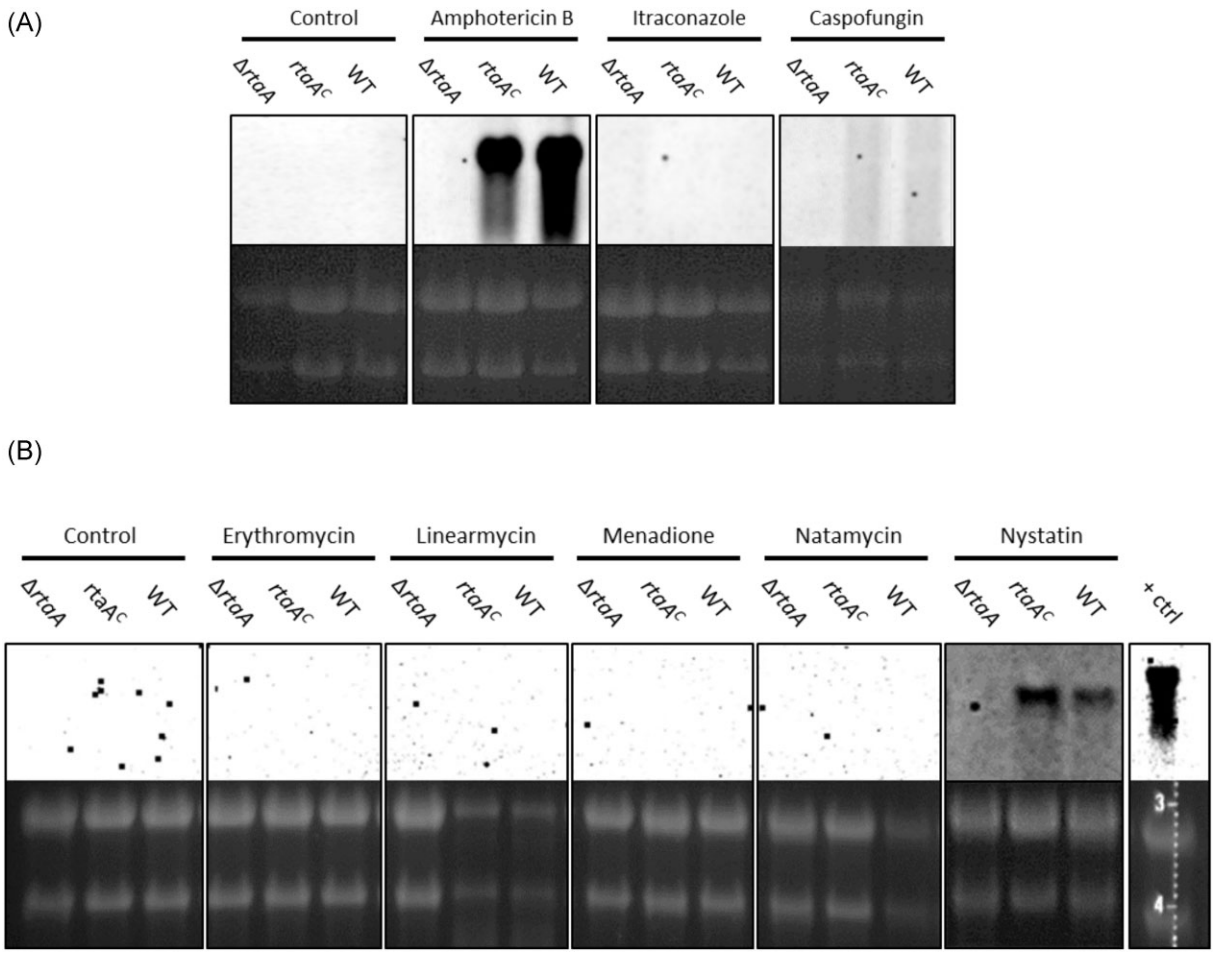

Figure 8. Analysis of expression of *rtaA* after exposure to AmB and nystatin. (A) Northern blot analysis of the expression of *rtaA* in *A. fumigatus* (Δ*rtaA*1, *rtaA*^{C}, and WT) after exposure to sublethal concentrations of the antifungals AmB, ITZ, or caspofungin. (B) Expression of *rtaA* in *A. fumigatus* after exposure to the *Streptomyces*-derived antibiotics erythromycin and linearmycin, ROS-forming Mnd, and the polyene macrolides natamycin and nystatin. Ribosomal RNA served as loading control in (A) and (B).

cellular processes, including membrane trafficking, lipid metabolism, and signalling (Rizzo et al. 2019). There are various models that attempt to explain how fungal flippases may be involved in drug resistance. One proposed mechanism involves the *S. cerevisiae* protein Rta1p, which confers resistance to 7-aminocholesterol. According to this model, Rta1p induces membrane internalization *via* the endocytic pathway and further transports the drug to vacuoles (Manente and Ghislain 2009). Another possibility is that deletion of a flippase gene leads to changes in the membrane composition resulting in an incorrect localization of the drug target, which increases sensitivity to the corresponding antifungal compound or disrupts membrane repair. Additionally, lipid flippases are necessary for intracellular vesicle trafficking, and any alterations in their activity or expression may affect various cellular processes such as membrane trafficking, lipid metabolism, and signalling (Shor et al. 2016). However, clear experimental evidence for a flippase function of Rta1p is still lacking.

To investigate whether *A. fumigatus* RtaA confers drug resistance to AmB *via* a mechanism similar to that proposed for the *S. cerevisiae* protein Rta1p, we stained the mycelium of *A. fumigatus* WT and Δ*rtaA* mutant hyphae with filipin, a fluorescent sterol marker used to monitor ergosterol content, and Nile red (Fig. 9, Fig. S8). Confocal laser scanning microscopy of both AmB-treated (0.04 and 0.08 µg/ml AmB) and untreated mycelia of *A. fumigatus* revealed a patchy distribution of filipin-derived fluorescence with higher intensity at septa and some hyphal tips (Fig. S8). A drastic difference in fluorescence intensity between WT and Δ*rtaA* hyphae could not be visually recognized (Fig. 9A). However, intensity-based image analysis (Fig. 9B) revealed a trend towards reduced filipin staining of Δ*rtaA* hyphae compared to the WT, which was, however, only significant in the presence of 0.04 µg/ml AmB ($P = .01$, Hedges' $g = 0.42$). We further performed LC–TQ–MS analysis to determine total cellular ergosterol levels. In accordance with the microscopic data, the Δ*rtaA* strain exhibited a decreased ergosterol content compared to the WT, and ergosterol was increased in the RtaA^{PXylP} strain upon xylose induction. Nevertheless, these differences were not statistically significant (Fig. 9C). In addition, we analysed the content of phytosphingosin and related sphingolipids, that have been discussed to contribute to AmB resistance (Madaan and Bari 2023). However, no significant differences were observed between the WT and the Δ*rtaA* mutant strain exposed to 0.125 mg/l AmB for 4 h or without treatment (Fig. S9).

As anticipated, Nile red staining highlighted intracellular lipid droplets, which were uniformly dispersed throughout the fungal hyphae. The treatment of hyphae with AmB led to a decrease in the median intensity of Nile red fluorescence at a higher drug concentration of 0.08 µg/ml AmB, and WT hyphae seemed to exhibit

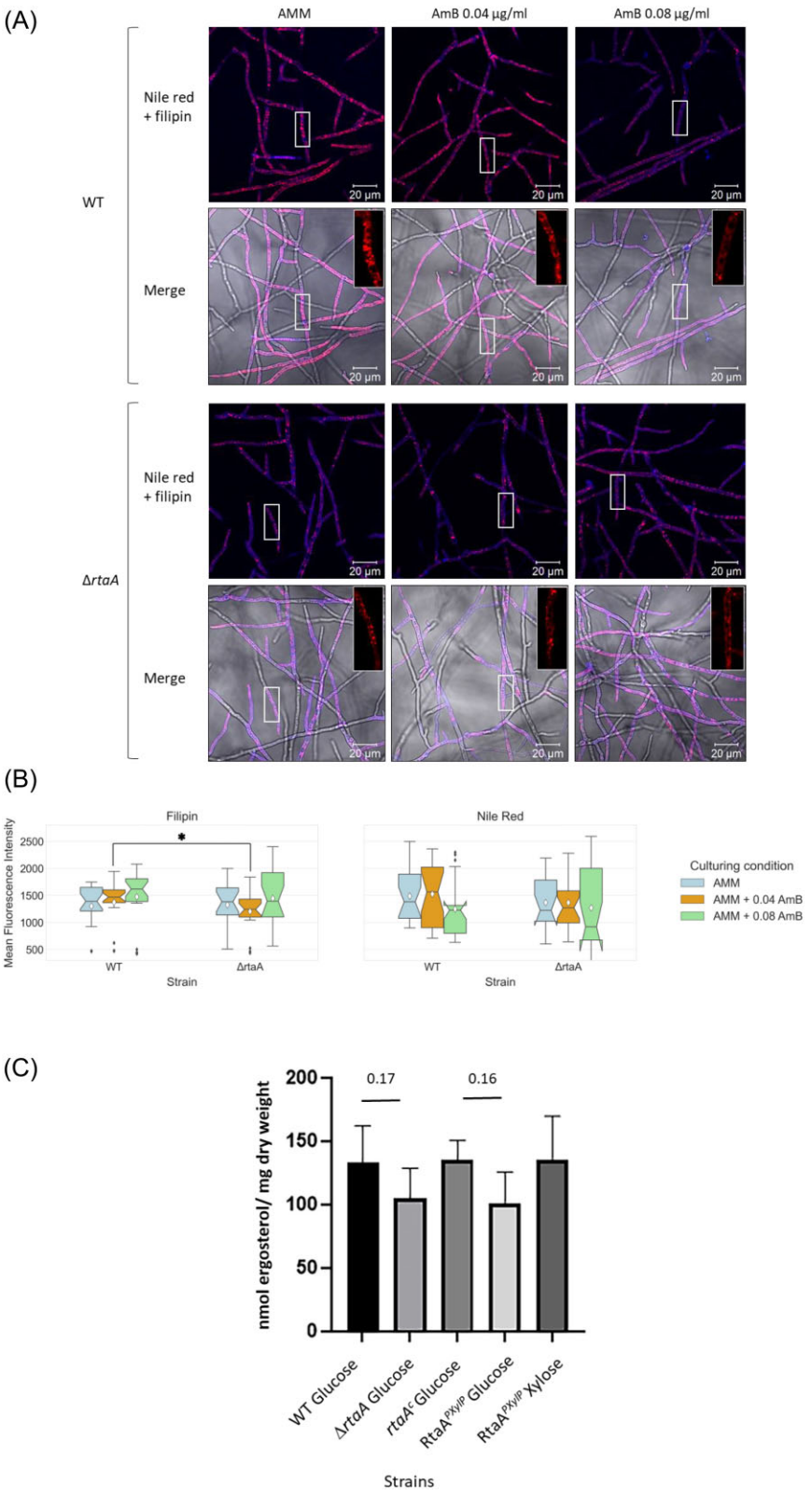

Figure 9. Filipin staining of the *rtaA* deletion mutant. (A) Hyphae of *A. fumigatus* WT and Δ*rtaA* treated or untreated with sublethal concentrations of AmB (0.04 and 0.08 µg/ml) were stained with filipin (detection of ergosterol) and Nile red (detection of lipid droplets) and investigated by confocal laser scanning microscopy. Scale bar = 20 µm. (B) Automated image analysis was used to quantify the average intensity values of Nile red and filipin in WT and Δ*rtaA* strains. The boxes in the graph represent quartiles centred around the median, where the median is represented by the line inside the box. The whiskers extend to the minimum and maximum values within a specific range, defined as 1.5 times the interquartile range above the upper quartile and below the lower quartile. Mean values are indicated by white diamonds on the graph. (C) LC–TQ–MS analysis of the ergosterol content by dry weight of the *A. fumigatus* WT strain and the mutant strains Δ*rtaA*, $rtaA^{C}$, and $RtaA^{PXylP}$ [cultivated under inducing (xylose)- and noninducing (glucose) conditions]. Values are based on three biological replicates.

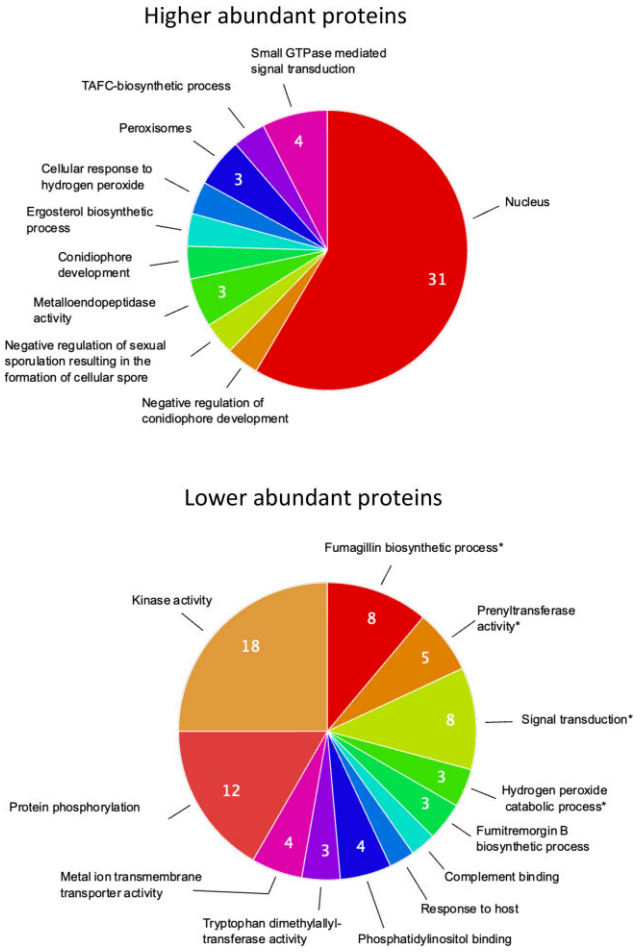

Figure 10. GO categorization of proteins with altered abundance in strain Δ*rtaA* in comparison to the WT after exposure to AmB (0.125 µg/ml) for 4 h. Proteins with abundance changes of >2- or <0.5-fold were included in the analysis using the web tool FungiFun 2 (https://elbe.hki-jena.de/fungifun/). Enriched GO terms are marked with an asterisk.

higher Nile red fluorescence signals in comparison to the Δ*rtaA* mutant, but all differences in Nile red staining were not significant in the intensity-based image analysis (Fig. 9A and B). A potential role of RtaA in lipid storage of mainly triacylglycerols and sterol esters and lipid trafficking is likely but needs further investigations. Alternatively, RtaA could be involved in a vesicle-dependent transport of AmB, the deletion of *rtaA* may alter the AmB drug response or RtaA simply stabilizes the membrane structure.

Deletion of *rtaA* alters the proteomic response of *A. fumigatus* to AmB

To investigate the impact of RtaA on the AmB stress response and to shed light on its possible protective functions, we compared the proteome of strain Δ*rtaA* exposed to 0.125 µg/ml AmB with the proteome of the WT strain. 399 different proteins decreased, and 264 proteins increased in abundance in comparison to the WT. PSEA revealed no GO term for proteins with higher abundance, but the terms fumagillin biosynthetic process, prenyltransferase activity, signal transduction, and hydrogen peroxide catabolic process for lower abundant proteins (Fig. 10, Table 3, and Table S8). These data suggest that the lack of RtaA leads to an increased disorganization of the cellular membrane resulting in impaired signalling processes and altered secondary metabolite production. Proteins with higher abundance included those which perform their function in the nucleus. In particular, proteins involved in DNA repair should be mentioned here (e.g. DNA repair proteins Swi10/Rad10 and Dds20/Mei5), which suggests that AmB may also induce directly or indirectly DNA damage.

Deletion of *rtaA* does not affect virulence in infected mice

To evaluate the impact of *rtaA* deletion on virulence, we employed two distinct pulmonary models of infection in immunocompromised mice. Three groups, each consisting of 10 mice, were infected with either WT, Δ*rtaA*, or *rtaA*^{c} conidia. In the first model, mice were immunocompromised with CA (CA model), while in the second model, mice were rendered neutropenic *via* administration of CP (CP model). Subsequently, mice were infected intranasally with *A. fumigatus* conidia. We monitored mouse survival over the course of 28 days. The results indicate that there was no significant difference in virulence between the three strains ($P > .10$), as shown by the survival curve (Fig. 11). Therefore, it can be concluded that RtaA does not play a role for the virulence of *A. fumigatus*.

Discussion

Aspergillus fumigatus poses a significant threat to individuals with a weakened immune system and underlying pulmonary conditions such as cystic fibrosis or chronic obstructive pulmonary disease (COPD). While triazoles are commonly used for initial treatment of IPA, an increasing rate of azole resistance has led to a shift towards fallback therapy with AmB, despite its associated side effects. Recent reports have shown a rise in clinical isolates of *A. fumigatus* exhibiting resistance to AmB (Ashu et al. 2018, Reichert-Lima et al. 2018, Fakhim et al. 2022), but research into the resistance mechanisms of *A. fumigatus* has been limited (Manavathu et al. 1998, Gautam et al. 2008, Furukawa et al. 2020). To address this gap, we hypothesized that conducting a detailed proteomic analysis following exposure to sublethal concentrations of AmB and AmBisome would reveal proteins involved in mediating resistance against these drugs. We discovered that exposure to sublethal concentrations of AmB or AmBisome is associated with changes in the abundances of proteins involved in oxidation–reduction processes, secondary metabolite biosynthesis, aromatic acid metabolism, and transmembrane transport. Similar effects have previously been documented for other fungi. The activation of transmembrane transport processes upon exposure to antifungals appears to be a common adaptive stress response in many fungi (Ribeiro et al. 2022). Similarly, the modification of amino acid metabolism during AmB adaptation has been reported in yeast (Ribeiro et al. 2022), while the induction of oxidation–reduction processes has been observed in fungi belonging to the *Fusarium* species complex (Castillo-Castaneda et al. 2020). The only published analysis of the *A. fumigatus* proteomic response to AmB to date was based on 2D-gel electrophoresis (2D-GE) and only shows a small overlap with our data. This may be explained by the different methods used (2D-GE versus LC–MS/MS) and the much longer incubation time of 24 h instead of 4 h (Gautam et al. 2008). Noteworthy is that the RtaA protein was not detected in this 2D-GE-based study, most probably due to the strong bias of 2D-GE against membrane proteins (Santoni et al. 2000). Nevertheless, transport proteins were also identified as an enriched category in this study. Furthermore, the level of L-ornithine aminotransferase Afu4g09140, which is involved in arginine degradation, in-

Table 3. Proteins with the highest changes in abundance in strain Δ*rtaA* versus WT upon AmB exposure.

Locus tag	-fold change (Δ*rtaA*/WT)	Description	GO category (biological process/molecular function)
AFUA_1G12560	1 348 002	Endo-beta-1,4-glucanase D (cellulose catalytic process)	Cellulose catabolic process
AFUA_1G03780	1 048 733	C6 finger domain protein	Regulation of DNA-templated transcription
AFUA_7G04120	558 215	DUF636 domain protein	–
AFUB_096690	442 369	C2H2-type domain-containing protein	–
AFUA_5G00710	341 911	GABA permease, putative	Transmembrane transporter activity
AFUA_8G03960	337 524	Uncharacterized protein	Anaphase-promoting complex-dependent catabolic process
AFUA_4G12530	318 829	Calcium transporter, putative	Intracellular ion homeostasis
AFUA_2G15240	286 021	Small oligopeptide transporter, OPT family	Peptide transport
AFUA_4G06260	269 878	Mating-type switch/DNA repair protein Swi10/Rad10	Double-strand break repair via single-strand annealing
AFUA_1G17460	205 354	C6 transcription factor, putative	Positive regulation of transcription by RNA polymerase II
AFUA_4G10860	188 182	Velvet domain-containing protein	Sporulation resulting in formation of a cellular spore
AFUA_5G09170	139 674	C2H2 finger domain protein	Regulation of transcription by RNA polymerase II
AFUA_5G05800	127 342	Signal peptidase complex subunit	Signal peptidase processing
AFUA_6G03160	90 888	NACHT domain protein	–
KXV57_001507	50 678	RING-type domain-containing protein	Protein ubiquitination
AFUA_1G12690	43 219	ABC multidrug transporter mdr4	Transmembrane transport
AFUA_6G03500	41 381	Fungal N-terminal domain-containing protein	Regulation of DNA-templated transcription
AFUA_4G08830	39 325	Telomere length regulator protein (Rif1),	Telomere maintenance
AFUA_4G01130	38 509	Dienelactone hydrolase family protein	–
AFUA_1G14695	38 427	DNA repair protein Dds20/Mei5, putative	DNA recombination
AFUA_2G13620	−62 806	Thiamine pyrophosphate enzyme, putative	Isoleucine/valine biosynthetic process
AFUA_8G00170	−79 071	Nonribosomal peptide synthetase 13	Fumitremorgin biosynthetic process
AFUA_3G08710	−102 354	Protein kinase domain-containing protein	Protein serine/threonine kinase activity
AFUA_4G14130	−107 595	ABC multidrug transporter, putative	Transmembrane transport
AFUA_5G14740	−118 837	Fucose-specific lectin	Carbohydrate binding
AFUA_7G04870	−128 175	Glutamine–serine–proline rich protein, putative	Outer membrane
KXV57_003843	−158 260	Uncharacterized protein	–
AFUA_5G08740	−186 451	Palmitoyltransferase pfa5	Protein targeting to membrane
AFUB_090520	−206 285	N-acetyltransferase, GNAT family, putative	Acyltransferase activity
AFUA_2G03990	−242 370	F-box domain-containing protein	–
AFUA_1G05510	−250 859	Vacuolar import and degradation protein	Protein targeting to vacuole
AFUA_6G05330	−258 166	Small ribosomal subunit protein uS10 m	Translation
AFUA_6G13110	−274 094	Dynactin subunit 6	Mitotic spindle organization
AFUA_1G01540	−281 007	Endonuclease/exonuclease/phosphatase family protein	Endonuclease activity
AFUA_8G00520	−290 191	Fumagillin beta-trans-bergamotene synthase af520	Fumagillin biosynthetic process
AFUA_3G05780	−292 237	GATA transcription factor LreA	Regulation of DNA-templated transcription
AFUA_3G00660	−409 952	Uncharacterized protein	–
AFUA_2G15790	−605 287	RNA polymerase II holoenzyme cyclin-like subunit Ssn8	Positive regulation of transcription by RNA polymerase II
AFUA_3G11170	−652 653	CP2 transcription factor, putative	Regulation of transcription by RNA pl
AFUA_3G12830	−1 563 620	RTA1 domain protein, putative	Membrane

creased in both studies. In contrast, Gautam et al. (2008) reported the upregulation of genes and proteins involved in the ergosterol biosynthesis pathway, which is considered as a resistance mechanism. However, in our study, we only observed a 5.7-fold increase in Erg3 expression specifically for AmBisome (Cavassin et al. 2021). Surprisingly, we did not find clear evidence of increased intracellular ROS production following AmB exposure, in contrast to the findings of Gautam et al. (2008) and other studies (Shekhova et al. 2017). The only increased ROS-detoxifying enzyme was a predicted glutathione S-transferase Afu2g17300. It is possible that oxidative stress may become more prominent after a longer exposure time or at higher concentrations of the drug. In agreement with this assumption, by using a fluorogenic ROS probe, significant levels of intracellular ROS were detected after a 45-min exposure to AmB concentrations above the MIC (Shekhova et al. 2017). Collectively, this suggests that ROS-induction of AmB is in particular concentration-dependent.

Interestingly, the proteomic response of *A. fumigatus* to AmB and AmBisome did not completely overlap. This is demonstrated by the specific increase in the levels of proteins involved in iron

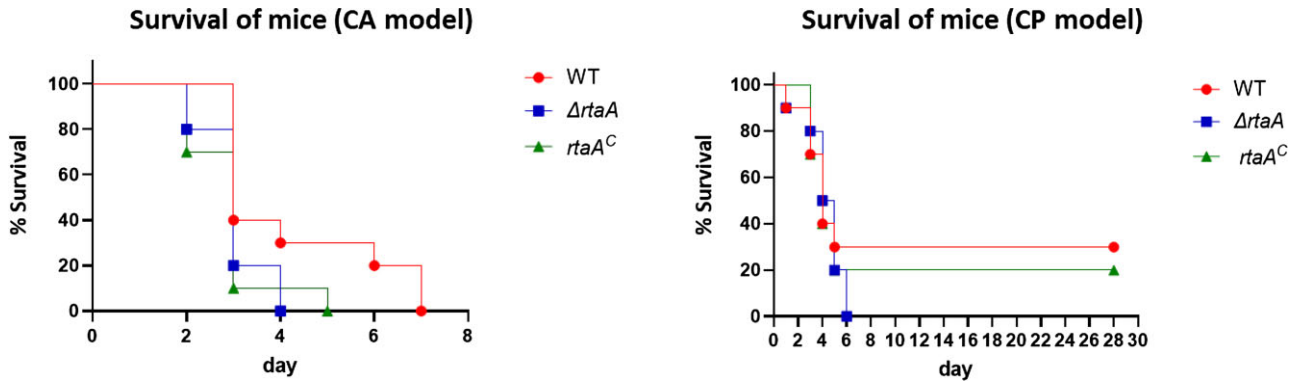

Figure 11. Analysis of virulence of the *rtaA* deletion mutant strain in mouse infection models. Survival rates of mice immunocompromised with CA alone (top graph) or CA and cyclophosphamide (CP, lower graph), and infected with *A. fumigatus* WT, Δ*rtaA*, or *rtaA*^{C}conidia, respectively. There were no statistically significant differences between the survival rates of the three groups. 10 mice were in each group.

homeostasis observed only upon exposure to AmBisome. This difference in proteomic response is likely due to the distinct delivery mechanisms of AmB and AmBisome. AmBisome penetrates the fungal cell wall, enabling direct delivery of AmB to the cell membrane (Walker et al. 2018). By contrast, AmB diffuses through the cell wall matrix, which influences the dynamics of membrane destabilization.

It is noteworthy that in our study, AmB and AmBisome specifically activated enzymes involved in the biosynthesis of secondary metabolites, such as the prenylated polyphenol fumicycline (also described as neosartoricins), as well as xanthocillin and hexadehydro-astechrome (HAS). The latter two secondary metabolites are known to form complexes with transition metals, and in case of HAS, contribute to the virulence of the fungus (Yin et al. 2013). A similar induction of secondary metabolite production by a natural product-based antifungal has also been reported in response to the lipopetide caspofungin, which triggers the production of fumagillin in *A. fumigatus* (Conrad et al. 2018). Therefore, it can be hypothesized that bacterial natural products with antifungal activity, such as AmB, have the potential to serve as specific inducers of secondary metabolite production in filamentous fungi. It provides another example that microbial natural products serve as communication signal during cross-kingdom interactions (Netzker et al. 2018, Scherlach and Hertweck 2020). AmB might even trigger the activation of an antimicrobial response program in *A. fumigatus*. For instance, the copper chelator xanthocillin has antibacterial activity (Raffa et al. 2021), suggesting that it may exert similar effects in response to AmB. Similarly, the iron chelator HAS (Yin et al. 2013) could potentially elicit comparable effects as well. Additionally, the putative antimicrobial peptide Afu8g00710 increased by 20–30-fold. More speculative is the assumption that the activation of the tyrosine and phenylalanine degradation pathway leads to the formation of pyomelanin that confers resistance to ROS and could enhance competitive fitness (Schmaler-Ripcke et al. 2009).

To identify genes involved in mediating resistance to AmB and AmBisome, we prioritized nine proteins with the highest upregulation in response to these drugs. These proteins were chosen as they likely play an active role in resistance against the stress caused by drug exposure, and their deletion may result in increased susceptibility. Of the nine genes studied, only the deletion of *rtaA*, encoding a putative fungal lipid-translocating exporter protein, resulted in increased susceptibility to AmB and AmBisome.

Our study thus highlights the potential role of RtaA in mediating modest resistance to AmB and AmBisome. The increased susceptibility to these drugs following *rtaA* deletion, as well as the increased resistance observed with *rtaA* overexpression, strongly suggest that RtaA is actively involved in conferring modest resistance to these drugs. Notably, this effect appears to be highly selective, as we observed no significant changes in sensitivity to other drugs or stressors. Additionally, our findings regarding the involvement of RTA-family member proteins in polyene resistance appear to be unique in *A. fumigatus* and related species when compared to other, phylogenetically distinct fungal species. For instance, *rta1* deletion in *S. cerevisiae* and *Cryptococcus neoformans* increased sensitivity to 7-amino cholesterol, a putative ergosterol biosynthesis inhibitor, without affecting sensitivity to other antifungals targeting sterol biosynthesis, including azoles and morpholine derivatives (Soustre et al. 1996, Smith-Peavler et al. 2022), while in *Candida albicans RTA2* and *RTA3* deletion led to azole susceptibility (Jia et al. 2008, Whaley et al. 2016).

Studies on *rta*-like family gene expression have been conducted in various fungal species including *S. cerevisiae*, *C. albicans*, and *C. glabrata*. In *S. cerevisiae*, *rta1* expression is triggered by hypoxia and cytotoxic stress (Kolaczkowska et al. 2012). In *C. albicans*, *RTA2* is induced by a wide range of cell membrane stressors including azoles, polyenes, and allylamines (Thomas et al. 2015), while in *C. glabrata*, *RTA1* induction was shown to be caused by hypoxia and azoles (Kolaczkowska et al. 2013). By contrast, we observed that *rtaA* expression was specifically induced by AmB and the similar polyene nystatin and not by other antifungal agents, such as ITZ or caspofungin. The lack of induction with the polyene natamycin may be explained with the possible different mode of action by binding specifically to ergosterol without permeabilizing the membrane (te Welscher et al. 2008).

To date, the mechanistic understanding of the RTA-like protein family function remains unclear, although, based on their similarity to the Rsb1 protein in yeast, it is assumed that they function as lipid translocases (Kihara and Igarashi 2004). Our work suggests that RtaA-dependent modulation of AmB sensitivity and resistance may result from changes in the membrane composition mediated *via* vesicular transport between lipid droplets and cell membrane. Lipid droplets may potentially act as a sink to remove AmB from the cytoplasmic membrane. Alternatively, RtaA may mediate the transport of the AmB target ergosterol or other membrane components between lipid droplets and the cellular membrane. The observation that RtaA localized to the cytoplasmic membrane was also shown for *S. cerevisiae* (Kolaczkowska et al.

2012), and partly one could observe an association of the RtaA-GFP signal with lipid droplets. No correlation was observed between the GFP signal and endosomal vacuoles, which contradicts the assumption that RtaA is involved in endocytic membrane transport processes. It cannot be ruled out that RtaA has also a protective function for other intracellular membranes (Higuchi 2021) or the overexpression of the GFP-fusion protein leads to mislocalization and degradation in vacuoles. In this context, it is noticeable that the treatment of *A. fumigatus* with the antifungal compound olorofim caused the formation of vesicle-like structures, which were not stainable with membrane- or vacuole-selective dyes (du Pre et al. 2020). It cannot be ruled out that RtaA accumulates in such structures besides its association with the cell membrane.

Taken together, in this study we conducted a detailed proteomic analysis to investigate the response of *A. fumigatus* to two commonly used antifungal drugs, AmB and AmBisome. Our results demonstrate that RtaA is the most upregulated protein in response to drug exposure and plays a role in resistance to polyenes, which is supported by the observation of a specific induction of *rtaA* expression by AmB and nystatin. Specifically, overexpression of RtaA confers resistance to AmB, AmBisome, and nystatin, while deletion of its encoding gene leads to increased sensitivity to these drugs. Our findings also suggest that RtaA is involved in lipid trafficking and storage to maintain lipid homeostasis. Furthermore, our study highlights the general importance of fungal RTA-like proteins in mediating resistance to compounds disturbing the integrity of the cell membrane.

The effect of RtaA deletion or overexpression on AmB drug susceptibility may be considered as modest (4-fold increase in susceptibility), but even small changes in MIC values can have a high impact on the success of an antifungal therapy as shown by a murine model of systemic aspergillosis with clinical isolates of *A. flavus* exhibiting different susceptibilities to AmB. Here, even small, increased AmB MIC levels of 2–4-fold resulted in failure of AmB and L-AmB treatment (Barchiesi et al. 2013).

An open question remains about how *rtaA* is regulated. Furukawa et al. (2020) showed that the negative cofactor 2 complex proteins NctA and NctB are key regulators of drug resistance and their loss leads to resistance against antifungal azoles, terbinafine, and AmB. However, it is unlikely that RtaA contributes to the observed AmB resistance, since both knock strains, Δ*nctA* and Δ*nctB*, showed reduced transcript levels of *rtaA* upon exposure to a sublethal concentration of ITZ.

It will be important to assess the clinical relevance of our findings by analysing the *rtaA* sequence and its expression in emerging AmB-resistant strains of *A. fumigatus* (Ashu et al. 2018, Reichert-Lima et al. 2018, Fakhim et al. 2022). In a recent study of *A. fumigatus* Single Nucleotide Polymorphisms in introns and exons of genes and their up- and downstream regions associated with AmB resistance, no correlation was found for the *rtaA* gene described here (Chen et al. 2023). In addition, we did not find difference in the expression levels of *rtaA* orthologues between strains of *A. lentulus* and *A. terreus* with different AmB-MIC values.

In summary, our data illustrates that RTA-like proteins fulfil an important function in specifically providing fungi with protection against membrane-interfering compounds and there is certainly more to discover. For example, it was recently shown that *Botrytis cinerea* employs an RTA-like protein to combat membrane-induced stress by plant-derived saponins (You et al. 2024).

Acknowledgements

We thank S. Steinbach for excellent technical assistance. We thank Mike Bromley (Manchester Fungal Infection Group) for providing two *A. fumigatus* knock-out strains of the genome-wide knockout program (COFUN) library.

Supplementary data

Supplementary data is available at *FEMSML Journal* online.

Conflict of interest: None declared.

Funding

This work was supported by Deutsche Forschungsgemeinschaft (DFG) within the Collaborative Research Centers (CRC)/Transregio 124 'FungiNet' to A.A.B., M.T.F., and O.K. (A1, B4, and Z2; project ID 210879364), CRC 1127 ChemBioSys (Project-ID 239748522), and CRC 1278 PolyTarget to A.A.B. and M.T.F. (B02 and Z01; project ID 316213987). Further support was received from the Israel-China Science Foundation (IFS) grant 2444/18 to N.O. . The work was further funded by the Federal Ministry of Education and Research (BMBF) in the funding program 'Zwanzig20–Partnerschaft für Innovation' (FINAR; FKZ 03ZZ0809A) and in the context of InfectoGnostics2 Research Campus Jena (ADA number 13GW0456B). Furthermore, M.T.F. and A.E.B. were funded by the Cluster of Excellence 'Balance of the Microverse—Project ID 390713860)'. The work of the German NRZMyk is supported by the Robert Koch Institute from funds provided by the German Ministry of Health (grant number 1369-240).

Data availability

The proteomic data that support the findings of this study are available from the ProteomeXchange Consortium via the PRIDE partner repository (Perez-Riverol et al. 2022) with dataset identifiers PXD042190 and PXD056876.

References

Ahmad S, Joseph L, Parker JE *et al. ERG6* and *ERG2* are major targets conferring reduced susceptibility to amphotericin B in clinical *Candida glabrata* isolates in Kuwait. *Antimicrob Agents Chemother* 2019;**63**:e01900–18.

Arastehfar A, Carvalho A, Houbraken J *et al. Aspergillus fumigatus* and aspergillosis: from basics to clinics. *Stud Mycol* 2021;**100**:100115.

Ashu EE, Korfanty GA, Samarasinghe H *et al.* Widespread amphotericin B-resistant strains of *Aspergillus fumigatus* in Hamilton, Canada. *Infect Drug Resist* 2018;**11**:1549–55.

Barchiesi F, Spreghini E, Sanguinetti M *et al.* Effects of amphotericin B on *Aspergillus flavus* clinical isolates with variable susceptibilities to the polyene in an experimental model of systemic aspergillosis. *J Antimicrob Chemother* 2013;**68**:2587–91.

Bode C, Graler MH. Quantification of sphingosine-1-phosphate and related sphingolipids by liquid chromatography coupled to tandem mass spectrometry. *Methods Mol Biol* 2012;**874**:33–44.

Brakhage AA, Van den Brulle J. Use of reporter genes to identify recessive trans-acting mutations specifically involved in the regulation of *Aspergillus nidulans* penicillin biosynthesis genes. *J Bacteriol* 1995;**177**:2781–8.

Brown GD, Denning DW, Gow NA *et al.* Hidden killers: human fungal infections. *Sci Transl Med* 2012;**4**:165rv113.

CaLS Institute. *Reference Method for Broth Dilution Antifungal Susceptibility Testing of Filamentous Fungi; Approved Standard*. Vol. **22**, Wayne PA: Clinical and Laboratory Standards Institute, 2008.

Carolus H, Pierson S, Lagrou K *et al.* Amphotericin B and other polyenes-discovery, clinical use, mode of action and drug resistance. *J Fungi* 2020;**6**:321.

Castillo-Castaneda A, Canas-Duarte SJ, Guevara-Suarez M *et al.* Transcriptional response of *Fusarium oxysporum* and *Neocosmospora solani* challenged with amphotericin B or posaconazole. *Microbiology* 2020;**166**:936–46.

Cavassin FB, Bau-Carneiro JL, Vilas-Boas RR *et al.* Sixty years of amphotericin B: an overview of the main antifungal agent used to treat invasive fungal infections. *Infect Dis Ther* 2021;**10**:115–47.

Chen F, Mackey AJ, Stoeckert CJ *et al.* OrthoMCL-DB: querying a comprehensive multi-species collection of ortholog groups. *Nucleic Acids Res* 2006;**34**:D363–368.

Chen MM, Shi GH, Dai Y *et al.* Identifying genetic variants associated with amphotericin B (AMB) resistance in *Aspergillus fumigatus* via k-mer-based GWAS. *Front Genet* 2023;**14**:1133593.

Conrad T, Kniemeyer O, Henkel SG *et al.* Module-detection approaches for the integration of multilevel omics data highlight the comprehensive response of *Aspergillus fumigatus* to caspofungin. *BMC Syst Biol* 2018;**12**:88.

da Silva Ferreira ME, Kress MR, Savoldi M *et al.* The *akuB*(KU80) mutant deficient for nonhomologous end joining is a powerful tool for analyzing pathogenicity in *Aspergillus fumigatus*. *Eukaryot Cell* 2006;**5**:207–11.

Denning DW. Global incidence and mortality of severe fungal disease. *Lancet Infect Dis* 2024;**24**:e428–e438.

du Pre S, Birch M, Law D *et al.* The dynamic influence of olorofim (F901318) on the cell morphology and organization of living cells of *Aspergillus fumigatus*. *J Fungi* 2020;**6**:47.

Edgar RC. MUSCLE: multiple sequence alignment with high accuracy and high throughput. *Nucleic Acids Res* 2004;**32**:1792–7.

Fakhim H, Badali H, Dannaoui E *et al.* Trends in the prevalence of amphotericin B-resistance (AmBR) among clinical isolates of *Aspergillus* species. *J Mycol Med* 2022;**32**:101310.

Furukawa T, van Rhijn N, Fraczek M *et al.* The negative cofactor 2 complex is a key regulator of drug resistance in *Aspergillus fumigatus*. *Nat Commun* 2020;**11**:427.

Gautam P, Shankar J, Madan T *et al.* Proteomic and transcriptomic analysis of *Aspergillus fumigatus* on exposure to amphotericin B. *Antimicrob Agents Chemother* 2008;**52**:4220–7.

Goedhart J, Luijsterburg MS. VolcaNoseR is a web app for creating, exploring, labeling and sharing volcano plots. *Sci Rep* 2020;**10**:20560.

Goncalves SS, Souza ACR, Chowdhary A *et al.* Epidemiology and molecular mechanisms of antifungal resistance in *Candida* and *Aspergillus*. *Mycoses* 2016;**59**:198–219.

Grimme SJ, Gao XD, Martin PS *et al.* Deficiencies in the endoplasmic reticulum (ER)-membrane protein Gab1p perturb transfer of glycosylphosphatidylinositol to proteins and cause perinuclear ER-associated actin bar formation. *Mol Biol Cell* 2004;**15**:2758–70.

Hallgren J, Tsirigos KD, Pedersen MD *et al.* DeepTMHMM predicts alpha and beta transmembrane proteins using deep neural networks. *bioRxiv* 2022.

Heberle H, Meirelles GV, da Silva FR *et al.* InteractiVenn: a web-based tool for the analysis of sets through Venn diagrams. *BMC Bioinf* 2015;**16**:169.

Higuchi Y. Membrane traffic in *Aspergillus oryzae* and related filamentous fungi. *J Fungi* 2021;**7**:534.

Imbert S, Normand AC, Cassaing S *et al.* Multicentric analysis of the species distribution and antifungal susceptibility of cryptic isolates from *Aspergillus* section *fumigati*. *Antimicrob Agents Chemother* 2020;**64**:e01374–20.

Itoh T, Tokunaga K, Matsuda Y *et al.* Reconstitution of a fungal meroterpenoid biosynthesis reveals the involvement of a novel family of terpene cyclases. *Nat Chem* 2010;**2**:858–64.

Jia XM, Ma ZP, Jia Y *et al.* RTA2, a novel gene involved in azole resistance in *Candida albicans*. *Biochem Biophys Res Commun* 2008;**373**:631–6.

Kihara A, Igarashi Y. Cross talk between sphingolipids and glycerophospholipids in the establishment of plasma membrane asymmetry. *Mol Biol Cell* 2004;**15**:4949–59.

Kolaczkowska A, Dylag M, Kolaczkowski M. Differential expression of the *Candida glabrata CgRTA1* and *CgRSB1* genes in response to various stress conditions. *Biochem Biophys Res Commun* 2013;**432**:169–74.

Kolaczkowska A, Manente M, Kolaczkowski M *et al.* The regulatory inputs controlling pleiotropic drug resistance and hypoxic response in yeast converge at the promoter of the aminocholesterol resistance gene *RTA1*. *FEMS Yeast Res* 2012;**12**:279–92.

König CC, Scherlach K, Schroeckh V *et al.* Bacterium induces cryptic meroterpenoid pathway in the pathogenic fungus *Aspergillus fumigatus*. *ChemBioChem* 2013;**14**:938–42.

Lim FY, Won TH, Raffa N *et al.* Fungal isocyanide synthases and xanthocillin biosynthesis in *Aspergillus fumigatus*. *mBio* 2018;**9**:e00785–18.

Livak KJ, Schmittgen TD. Analysis of relative gene expression data using real-time quantitative PCR and the 2(-Delta Delta C(T)) method. *Methods* 2001;**25**:402–8.

Lourenço-Silva J, Menezes MN, Rodrigues T *et al.* Encoder-decoder architectures for clinically relevant coronary artery segmentation. In: *Computational Advances in Bio and Medical Sciences*. Lecture Notes in Computer Science. Vol. **13254**. Cham: Springer, 2022.

Madaan K, Bari VK. Emerging role of sphingolipids in amphotericin B drug resistance. *Microb Drug Resist* 2023;**29**:319–32.

Manavathu EK, Alangaden GJ, Chandrasekar PH. *In-vitro* isolation and antifungal susceptibility of amphotericin B-resistant mutants of *Aspergillus fumigatus*. *J Antimicrob Chemother* 1998;**41**:615–9.

Manente M, Ghislain M. The lipid-translocating exporter family and membrane phospholipid homeostasis in yeast. *FEMS Yeast Res* 2009;**9**:673–87.

Martel CM, Parker JE, Bader O *et al.* A clinical isolate of *Candida albicans* with mutations in *ERG11* (encoding sterol 14alpha-demethylase) and *ERG5* (encoding C22 desaturase) is cross resistant to azoles and amphotericin B. *Antimicrob Agents Chemother* 2010;**54**:3578–83.

Mikołajczyk A, Grochowski M. Data augmentation for improving deep learning in image classification problem. In: *Proceedings of the 2018 International Interdisciplinary PhD Workshop*. Piscataway, NJ: IEEE, 2018.

Minh BQ, Schmidt HA, Chernomor O *et al.* IQ-TREE 2: new models and efficient methods for phylogenetic inference in the genomic era. *Mol Biol Evol* 2020;**37**:1530–4.

Myers EW, Miller W. Optimal alignments in linear space. *Comput Appl Biosci* 1988;**4**:11–17.

Netzker T, Flak M, Krespach MK *et al.* Microbial interactions trigger the production of antibiotics. *Curr Opin Microbiol* 2018;**45**:117–23.

Paysan-Lafosse T, Blum M, Chuguransky S *et al.* InterPro in 2022. *Nucleic Acids Res* 2023;**51**:D418–27.

Perez-Riverol Y, Bai J, Bandla C *et al.* The PRIDE database resources in 2022: a hub for mass spectrometry-based proteomics evidences. *Nucleic Acids Res* 2022;**50**:D543–52.

Priebe S, Kreisel C, Horn F *et al.* FungiFun2: a comprehensive online resource for systematic analysis of gene lists from fungal species. *Bioinformatics* 2015;**31**:445–6.

Raffa N, Won TH, Sukowaty A *et al.* Dual-purpose isocyanides produced by *Aspergillus fumigatus* contribute to cellular copper sufficiency and exhibit antimicrobial activity. *Proc Natl Acad Sci USA* 2021;**118**:e2015224118.

Reichert-Lima F, Lyra L, Pontes L *et al.* Surveillance for azoles resistance in *Aspergillus* spp. highlights a high number of amphotericin B-resistant isolates. *Mycoses* 2018; **61**:360–5.

Ribeiro GF, Denes E, Heaney H *et al.* What 'Omics can tell us about antifungal adaptation. *FEMS Yeast Res* 2022;**21**:foab070.

Rizzo J, Stanchev LD, da Silva VKA *et al.* Role of lipid transporters in fungal physiology and pathogenicity. *Comput Struct Biotechnol J* 2019;**17**:1278–89.

Ronneberger O, Fischer P, Brox T. U-net: convolutional networks for biomedical image segmentation. In: *Proceedings of the Medical Image Computing and Computer-Assisted Intervention – MICCAI 2015*. Lecture Notes in Computer Science. Vol. **9351**. Cham: Springer, 2015.

Santoni V, Molloy M, Rabilloud T. Membrane proteins and proteomics: un amour impossible?. *Electrophoresis* 2000;**21**:1054–70.

Scherlach K, Hertweck C. Chemical mediators at the bacterial–fungal Interface. *Annu Rev Microbiol* 2020;**74**:267–90.

Schmaler-Ripcke J, Sugareva V, Gebhardt P *et al.* Production of pyomelanin, a second type of melanin, via the tyrosine degradation pathway in *Aspergillus fumigatus*. *Appl Environ Microbiol* 2009;**75**:493–503.

Shashkova S, Welkenhuysen N, Hohmann S. Molecular communication: crosstalk between the Snf1 and other signaling pathways. *FEMS Yeast Res* 2015;**15**:fov026.

Shekhova E, Kniemeyer O, Brakhage AA. Induction of mitochondrial reactive oxygen species production by itraconazole, terbinafine, and amphotericin B as a mode of action against *Aspergillus fumigatus*. *Antimicrob Agents Chemother* 2017;**61**:e00978–17.

Shor E, Wang Y, Perlin DS *et al. Cryptococcus* flips its lid—membrane phospholipid asymmetry modulates antifungal drug resistance and virulence. *Microb Cell* 2016;**3**:358–60.

Shorten C, Khoshgoftaar TM. A survey on image data augmentation for deep learning. *J Big Data* 2019;**6**:60.

Smith-Peavler ES, Patel R, Onumajuru AM *et al. RTA1* is involved in resistance to 7-aminocholesterol and secretion of fungal proteins in *Cryptococcus neoformans*. *Pathogens* 2022;**11**:1239.

Soustre I, Letourneux Y, Karst F. Characterization of the *Saccharomyces cerevisiae RTA1* gene involved in 7-aminocholesterol resistance. *Curr Genet* 1996;**30**:121–5.

Steenwyk JL, Buida TJ, Li Y *et al.* ClipKIT: a multiple sequence alignment trimming software for accurate phylogenomic inference. *PLoS Biol* 2020;**18**:e3001007.

Stroe MC, Netzker T, Scherlach K *et al.* Targeted induction of a silent fungal gene cluster encoding the bacteria-specific germination inhibitor fumigermin. *eLife* 2020;**9**:e52541.

Tan M, Le QV. EfficientNet: rethinking model scaling for convolutional neural networks. In: *Proceedings of the 36th International Conference on Machine Learning, ICML 2019*. San Diego CA: ICML, 2019, 6105–14

te Welscher YM, ten Napel HH, Balagué MM *et al.*. Natamycin blocks fungal growth by binding specifically to ergosterol without permeabilizing the membrane. *J Biol Chem* 2008;**283**:6393–401.

Thomas E, Sircaik S, Roman E *et al.* The activity of *RTA2*, a downstream effector of the calcineurin pathway, is required during tunicamycin-induced ER stress response in *Candida albicans*. *FEMS Yeast Res* 2015;**15**:fov095.

Vincent BM, Lancaster AK, Scherz-Shouval R *et al.* Fitness trade-offs restrict the evolution of resistance to amphotericin B. *PLoS Biol* 2013;**11**:e1001692.

Walker L, Sood P, Lenardon MD *et al.* The viscoelastic properties of the fungal cell wall allow traffic of AmBisome as intact liposome vesicles. *mBio* 2018;**9**:e02383–17.

Wessel D, Flugge UI. A method for the quantitative recovery of protein in dilute solution in the presence of detergents and lipids. *Anal Biochem* 1984;**138**:141–3.

Whaley SG, Tsao S, Weber S *et al.* The *RTA3* gene, encoding a putative lipid translocase, influences the susceptibility of *Candida albicans* to fluconazole. *Antimicrob Agents Chemother* 2016;**60**:6060–6.

Yin WB, Baccile JA, Bok JW *et al.* A nonribosomal peptide synthetase-derived iron(III) complex from the pathogenic fungus *Aspergillus fumigatus*. *J Am Chem Soc* 2013;**135**:2064–7.

You Y, Suraj HM, Matz L *et al.* Botrytis cinerea combines four molecular strategies to tolerate membrane-permeating plant compounds and to increase virulence. *Nat Commun* 2024;**15**:6448.

Yu G. Using ggtree to visualize data on tree-like structures. *Curr Protoc Bioinformatics* 2020;**69**:e96.

Zhou Z, Rahman Siddiquee MM, Tajbakhsh N *et al.* Unet++: a nested U-Net architecture for medical image segmentation. In: *Deep Learning in Medical Image Analysis and Multimodal Learning for Clinical Decision Support*. Lecture Notes in Computer Science. Vol. **11045**. Cham: Springer, 2018.

Received 20 June 2024; **revised** 19 November 2024; **accepted** 4 December 2024